Exoplanet atmospheres at high spectral resolution

Snellen, I.A.G.

ANNUAL REVIEWS

Annual Review of Astronomy and Astrophysics

Exoplanet Atmospheres at High Spectral Resolution

Ignas A.G. Snellen

Leiden Observatory, Leiden University, Leiden, The Netherlands;
email: snellen@strw.leidenuniv.nl

Annu. Rev. Astron. Astrophys. 2025. 63:83–125

First published as a Review in Advance on May 14, 2025

The *Annual Review of Astronomy and Astrophysics* is online at astro.annualreviews.org

https://doi.org/10.1146/annurev-astro-052622-031342

Keywords

spectroscopic techniques, planet formation, atmospheric chemistry, atmospheric dynamics

Abstract

High-resolution spectroscopy (HRS) has grown into one of the main techniques for characterizing the atmospheres of extrasolar planets. High spectral resolving power allows for the efficient removal of telluric and host-star contamination. Combined with the large collecting area of ground-based telescopes, it enables detailed studies of atmospheric species, temperature structure, atmospheric loss, and global winds and circulation patterns. In this review, the wide range of HRS observation and data analysis techniques are described and literature results discussed. Key findings include the following:

- The highest irradiated planets show a rich spectrum of atomic and ionic species, just like stars.
- Retrieval analyses of hot Jupiters and directly imaged super-Jupiters point to solar metallicities and chemistry, but observed samples are still heterogeneous and incomplete.
- There appears to be a clear dichotomy between hot Jupiters with and without atmospheric inversions, depending on their equilibrium temperature.
- Some highly irradiated planets exhibit enormous leading and/or trailing tails of helium gas, providing unique insights into planet evolution and atmospheric escape processes.
- Minor isotopes of carbon and oxygen are now being detected in gas giant planets and brown dwarfs with the interesting potential to shed light on formation pathways.

A list of potential pitfalls is provided for those new to the field, and synergies with the *James Webb Space Telescope* are discussed. HRS has a great future ahead with the advent of the extremely large telescopes, promising to bring temperate rocky exoplanets into view with their increase in HRS detection speed of up to three orders of magnitude.

Contents

1. INTRODUCTION

Since the discovery of the first extrasolar planets in the early 1990s, thousands of new worlds have been discovered. Although the census of planetary systems is yet far from complete, it is clear that exoplanets are both common and diverse. They can be found in orbits of less than a day but also at hundreds of astronomical units from their host star, and their masses and radii point to a broad continuum in compositions. Evidently, our Solar System is not a universal blueprint for other planetary systems.

An important goal of exoplanet studies is to understand the formation and evolutionary processes driving this diversity. This also enlightens us about the worlds in our own Solar System, e.g., explaining why Earth and Venus are so different or how planetary climates have evolved over time. Only by studying a wide variety of worlds—over a wide range of orbits, host-star properties, ages, and compositions—will we be able to identify families or classes of planets and understand their formation and evolutionary relationships. This also has a strong philosophical component with a unique opportunity to learn about ourselves as highly evolved organisms living on a

temperate, water-rich world. How common are life-bearing planets? Are there any other worlds like Earth?

Some basic properties of exoplanets can be constrained using indirect detection methods, such as planet mass from radial velocity (RV) measurements, radius from transit observations, and mean density from the combination of the two. The latter can put constraints on a planet's bulk composition, but solutions are often highly degenerate and atmospheric measurements are required to gain more detailed knowledge on chemical make-up and local conditions. The first question that can be addressed is whether a planet has an atmosphere or not. Subsequently, we want to know its chemical ingredients and temperature structure. Do we understand the physical and chemical processes in the context of its formation and evolution? In the search for habitable environments and extraterrestrial life, we want to know whether there is evidence for water. Can we detect any potential biomarker gases, such as molecular oxygen, ozone, or methane? And ultimately, are these biomarkers indeed due to biological activity?

Although space-based observations kick-started the field of atmospheric characterization more than two decades ago, ground-based high-resolution spectroscopy (HRS) has slowly but surely developed into a remarkable and unique way to probe exoplanets and forms the focus of this review. In the remainder of Section 1, a brief history of exoplanet atmospheric observations is presented, followed by an overview of the wide range of HRS observing methods. Section 2 provides technical details on HRS instrumentation, data acquisition, signal search techniques, and retrieval analyses. Section 3 discusses results for short-period planets that have been presented in the literature so far using HRS transmission and phase-curve measurements. Section 4 discusses these for directly imaged planets for which HRS is combined with high-contrast imaging (HCI) techniques. Section 5 examines synergies with *James Webb Space Telescope* (JWST) observations, and Section 6 discusses the exciting future of HRS in the era of the extremely large telescopes (ELTs).

A graduate-level review on HRS for exoplanet atmospheres has been presented before by Birkby (2018). The general review on exoplanet atmospheres by Madhusudhan (2019) is also a great source of information.

1.1. A Brief History of Exoplanet Atmospheric Observations

After the discovery of two planetary-mass objects orbiting a pulsar (Wolszczan & Frail 1992), it was the detection of the first hot Jupiter by Mayor & Queloz (1995) that started a genuine scientific revolution. Significant skepticism existed in the early days, because it was not generally accepted that the observed RV variations were caused by orbiting planets (e.g., Gray 1997). This resulted in a strong incentive to search for other evidence for exoplanets, in particular starlight scattered off their atmospheres (Charbonneau et al. 1999, Collier Cameron et al. 1999). Although unsuccessful, these attempts constitute the first time HRS was utilized to search for atmospheric signals. At high spectral resolution, reflected light can be disentangled from direct starlight due to its Doppler shift caused by the orbital motion of a planet. Unfortunately, hot Jupiters turn out to have very low albedos, and no undisputed HRS scattered-light signals have been found so far.

The groundbreaking discovery that the hot Jupiter HD 209458b transits its host star (Charbonneau et al. 2000) opened the way for a new technique: exoplanet transmission spectroscopy (Seager & Sasselov 2000). Subsequently, Charbonneau et al. (2002) detected sodium in transmission using the *Hubble Space Telescope* (HST)'s Space Telescope Imaging Spectrograph (STIS), which started a new subfield of exoplanet atmosphere measurements. In the years that followed, space-observations with both HST and the *Spitzer Space Telescope* were trailblazing. Charbonneau et al. (2005) and Deming et al. (2005b) presented the first secondary eclipse measurements of thermal emission using *Spitzer*, followed by the first infrared phase-curve and

longitudinal heat distribution (Knutson et al. 2007). HST observations in UV light showed significant Lyman-α (Lyα) and metallic transmission signals out to at least several planet radii, pointing to exospheric absorption and atmospheric loss processes (Vidal-Madjar et al. 2003, 2004). Absorption from water vapor turned out to be more elusive, and early claims (e.g., Tinetti et al. 2007) were disputed, until water measurements became irrefutable with HST's Wide-Field Camera 3 (WFC3) instrument (e.g., Deming et al. 2013). Until the launch of the JWST (see Section 5), the HST has been pushing the frontier of atmospheric characterization by inferring hazes from hot-Jupiter spectra (Sing et al. 2016), high-precision transmission spectroscopy of the mini-Neptune GJ 1214 (Kreidberg et al. 2014), and cool planets such as K2-18b (Benneke et al. 2019), and many other results.

In the meantime, theoretical studies showed the exciting possibilities of ground-based HRS transmission spectroscopy (e.g., Brown 2001), but early attempts resulted in upper limits (Moutou et al. 2001, Wiedemann et al. 2001, Deming et al. 2005a). The first successful ground-based observations targeted the sodium D lines in HD 189733b and HD 209458b using the Hobby–Eberly Telescope (Redfield et al. 2008) and the Subaru Telescope (Snellen et al. 2008), respectively, the latter confirming the earlier HST detection. Although sodium has been detected in many hot Jupiters since, recent observations of HD 209458 have cast some doubts on these early results (Casasayas-Barris et al. 2021) (see Section 3.1), mostly owing to the treatment of stellar-related contaminants.

Subsequently, the cryogenic high resolution IR Echelle Spectrometer (CRIRES) on the European Southern Observatory (ESO)'s Very Large Telescope (VLT) was used to detect carbon monoxide in the transmission spectrum of HD 209458b (Snellen et al. 2010), successfully utilizing cross-correlation (CC) techniques for the first time. It demonstrated the unique capabilities of HRS compared to space-based low-resolution spectroscopy by the unambiguous detection of a molecular signal and revealing Doppler effects of planet orbital motion and possible atmospheric winds. The change in the radial component of the orbital velocity of a planet was subsequently used to target thermal emission of the nontransiting planet Tau Boötis b (Brogi et al. 2012, Rodler et al. 2012), detecting carbon monoxide and revealing its orbital inclination, followed by the first ground-based detection of water in the thermal spectrum of HD 189733b (Birkby et al. 2013).

An alternative route for characterizing exoplanet atmospheres opened up through the first detections of substellar companions using HCI (e.g., Chauvin et al. 2004, Marois et al. 2008, Lagrange et al. 2010). These super-Jupiters are typically massive gas giants that straddle the planet–brown dwarf divide, residing on wide orbits in young (<100 Myr) star systems, and are almost solely in the observational realm of large ground-based telescopes with state-of-the-art adaptive optics (AO) systems. Because every measurement directly probes such objects, atmospheric characterization is immediate upon discovery and can be supplemented by observations at different wavelengths or by high-contrast spectroscopy. In this way, the dominant spectroscopically active species, such as water, carbon monoxide, and methane, are readily observable in super-Jupiters (e.g., Bowler et al. 2010), and the atmospheric temperature structure and possible presence of clouds is constrained. Because the spectroscopic signatures of stars and their planets are significantly different, many studies have recognized the power of combining HCI with HRS (e.g., Sparks & Ford 2002, Riaud & Schneider 2007, Kawahara & Hirano 2014, Snellen et al. 2015). Konopacky et al. (2013) first demonstrated the strength of medium-resolution integral-field spectroscopy on the HR 8799 system with the 10-m Keck OH-Suppressing Infrared Integral Field Spectrograph (OSIRIS). Subsequently, CRIRES was used to target the massive gas-giant Beta Pictoris b, measuring the radial component of its orbital velocity and deriving its spin-rotation period via its $v \sin i$ (Snellen et al. 2014).

Over the years, HRS has developed into an established observational technique for exoplanet atmospheric characterization. In the current JWST era, which provides unprecedented and unrivaled capabilities in particular in the thermal IR, ground-based HRS remains uniquely competitive and highly synergetic with space-based observations (see Section 5); e.g., HRS observations show that the optical spectra of the highest irradiated gas giants are dominated by neutral and ionized metals (Hoeijmakers et al. 2019), with dayside spectra suggesting strong thermal inversions (Nugroho et al. 2020a). Atmospheric escape processes can now be probed very effectively at high spectral resolution using the helium 1083-nm line (Allart et al. 2018, Nortmann et al. 2018). A strong synergy is developing between spatially resolved HRS observations that reveal signatures of dayside-to-nightside winds, zonal flows, and other atmospheric dynamics, and 3D atmospheric modeling (Louden & Wheatley 2015). HRS of directly imaged super-Jupiters have allowed for the first isotope measurements (Zhang et al. 2021). As discussed in Section 6, soon the ELTs will further revolutionize the field of HRS atmospheric characterization, ultimately opening up characterization of temperate rocky planets.

1.2. Overview of High-Resolution Spectroscopic Methods

Any atmospheric measurement requires radiation originating from the planet to be distinguished from that of the host star. Basically, there are two families of methods that can achieve this: time-differential observations, where contributions from the planet change over time (e.g., during transit or eclipse, or with phase-curve observations; technical details discussed in Section 2.2), or angular separation of the planet from the star (e.g., direct imaging, HCI, or interferometric observations). **Figure 1** shows a diagram (cf. Perryman 2000) of the wide range of methods utilizing HRS to target exoplanet atmospheres and which properties can be measured now or possibly in the future.

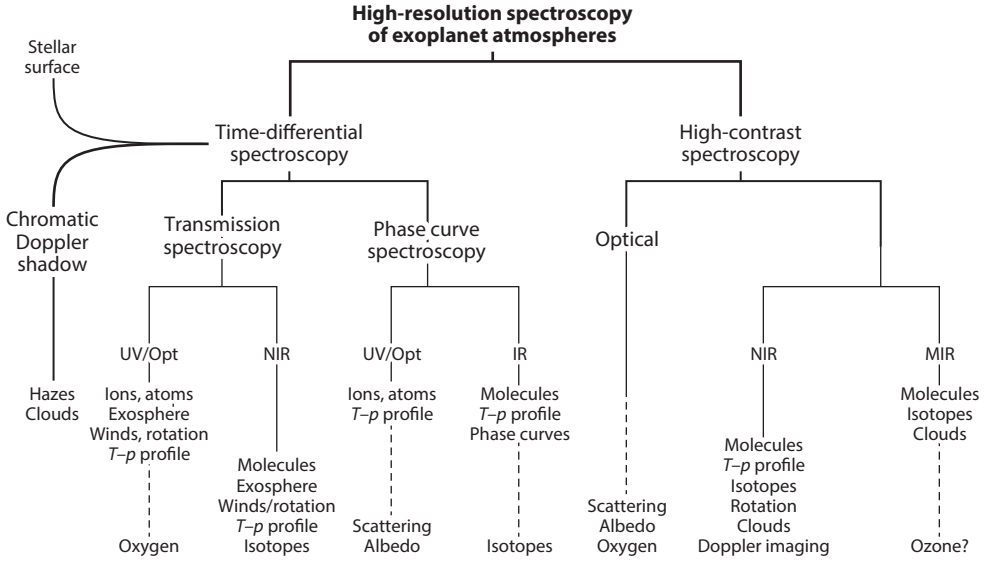

Figure 1

Diagram showing the range of methods employed to probe exoplanet atmosphere using high-resolution spectroscopy. The specific atmospheric properties that can be studied are indicated per wavelength regime. Dotted lines indicate future possibilities. Figure inspired by Perryman (2000).

Transmission spectroscopy measures the integrated light from the planet–star system during transit as a function of wavelength (e.g., Madhusudhan 2019). Absorption and scattering processes make the transparency of the atmosphere dependent on wavelength and, as such, impact the effective planet size and transit depth. With HRS, the transmission spectrum is also sensitive to Doppler effects induced by the planet orbital motion and atmospheric dynamics such as dayside-to-nightside winds, equatorial jet streams, or bulk rotation. The transmission signal from a specific atmospheric species depends on its abundance as a function of altitude in the atmosphere, the abundances of other species that may shield its signal, and the atmospheric temperature structure that is influenced by the surface gravity and mean molecular weight of the atmosphere. In the UV–optical wavelengths, transmission signals generally come from atoms and ions originating from the hydrostatic part of the atmosphere or an extended exosphere that may indicate atmospheric escape. Transmission spectroscopy in the near-IR (NIR) is mainly sensitive to molecular absorption, but exospheric helium can also be targeted.

During transit, the Rossiter–McLaughlin effect (RM or Doppler shadow) induced by a planet, which is widely used to measure spin-orbital alignments, can also be used to obtain a transmission spectrum (Snellen 2004, Dreizler et al. 2009, Santos et al. 2020). The amplitude of the RM effect (measured using stellar lines) depends on the effective size of the planet, which is affected by atmospheric absorption and scattering as above. By measuring chromatic variations in the RM effect, broadband transmission features can be determined, which are mostly inaccessible via classical HRS transmission spectroscopy. During transit, information can also be obtained on the spectrum of the local stellar surface that is being transited, such as star spots and center-to-limb variations (CLVs) in stellar line shapes and strengths (Cegla et al. 2016). The combined effects of the Doppler shadow, CLV, and planet atmospheric absorption can be very challenging to disentangle.

Phase-curve observations are time-differential measurements away from the transit, during which the planet is seen from different viewing angles. In contrast to transmission spectroscopy, nontransiting planets can also be targeted. While in the latter case constraints on the planet radius are missing, the HRS phase curve yields the orbital inclination of the planet and therefore the true mass. As for transmission spectroscopy, IR phase-curve observations are dominated by molecular opacity sources. The temperature structure, i.e., temperature–pressure (T–p) profile of the atmosphere, governs how molecular opacity is translated into the observed spectrum. An isothermal atmosphere produces (to first order) a black body spectrum without atomic or molecular lines. An atmosphere with an inverted or noninverted T–p profile results in emission or absorption lines, respectively. In the UV/optical wavelengths, the contrast between thermal emission from the planet and from the star is generally very large. Only the hottest planets (i.e., ultra-hot Jupiters or UHJs) can currently be studied in this way. They show mainly opacity from atoms and ions but potentially also metal oxides and metal hydrides. For all but the hottest planets, the UV/optical light is likely dominated by starlight scattered off the planet, but no undisputed HRS detections have yet been presented in the literature. If the size of the planet is known (i.e., for transiting planets), scattered light leads to the geometric albedo of the planet as a function of wavelength, providing insights in scattering processes (Rayleigh, Mie) and possibly the scattering medium (clouds, hazes, molecules). Depending on the effective range of altitudes at which the starlight is being scattered, light travels back and forth through the planet atmosphere, but it is also being absorbed, meaning that also the scattered light spectrum contains information on atmospheric constituents.

In the case of high-contrast spectroscopy (branch to the right in **Figure 1**), HCI techniques are combined with HRS. Light from the star is removed as much as possible at the position of the planet to obtain its spectrum free from stellar contamination. It requires an AO-assisted HRS spectrograph, possibly in conjunction with coronagraphy. In principle, this technique can also be used in combination with interferometry, but no HRS modes yet exist for such instruments.

So far, all directly imaged planets amenable to HRS observations have more favorable planet–star contrasts because they are young and still warm from their formation. Because they are only detectable in relatively wide orbits, their spectra are completely dominated by thermal emission, and reflected starlight is negligible. As with phase-curve observations, their HRS spectra provide information on molecular species, atmospheric T–p profile, and the possible presence of clouds. Recently, the first isotopic measurements have also been obtained (Zhang et al. 2021). Planet spin-rotation can be constrained using line broadening. Potentially, spatially resolved information of planets may be obtained, revealing possible dark or bright spots or bands, using Doppler imaging (Crossfield 2014). These require highly accurate HRS spectral time series.

In the era of the ELTs, HRS instrumentation should improve sufficiently to target planets around our nearest-neighbor stars in reflected light, providing constraints on albedo and atmospheric constituents at optical/NIR wavelengths. Arguably the holy grail in exoplanet science is the search for extraterrestrial life via biomarker gases. Molecular oxygen is potentially detectable in atmospheres of nearby rocky exoplanets using either HRS transmission spectroscopy or high-contrast spectroscopy (e.g., Lovis et al. 2017).

2. DETAILED TECHNIQUES

In this section, HRS observing and data analysis techniques are described in detail. First, the relevant properties of HRS instrumentation are discussed; then we discuss how they influence detection speed and how existing and planned HRS instruments compare to each other. Section 2.2 reviews observation and data analysis strategies, Section 2.3 examines the many aspects of atmospheric modeling, and Section 2.4 provides a list of potential pitfalls.

2.1. High-Resolution Spectroscopy Instrumentation

Over the past decades, there has been an enormous incentive to develop stable, high-precision, high-resolution spectrographs for the search of extrasolar planets using the RV technique. These same instruments are utilized for exoplanet atmospheric observations. Only in recent years have instruments been developed with atmospheric work as their main science driver (e.g., Mawet et al. 2016, Vigan et al. 2024). A key property is the detection speed, Γ, which governs the observing time needed to achieve a detection of a certain atmospheric species at a set signal-to-noise (S/n) ratio. Here, three very simplified cases, A, B, and C, are discussed.

In case A, the target spectrum consists of a set of well-separated, infinitely narrow lines of equal strength. Assuming a telescope diameter D and a telescope+instrument throughput of f, the detection speed is proportional to

$$\Gamma_{\mathrm{A}} \propto D^2 f \lambda_{\mathrm{span}} R, \qquad 1.$$

where R is the resolving power and λ_{span} is the instantaneous wavelength coverage of the spectrograph. Note that this is only a gross simplification of reality for many reasons, because this would imply that one should always push for the largest resolving power and wavelength coverage. First of all, λ_{span} and R are generally not independent from each other owing to the limited detector space. Also, the throughput f of a spectrograph typically decreases with increasing R, which depends on its instrumental design, level of atmospheric turbulence, and the presence and performance of a possible AO system. A higher R generally makes telluric line removal more effective, and a minimum R is needed to measure certain physical characteristics, such as thermal line broadening, spin rotation, or planet orbital velocity. In addition, a higher R means that lines are less blended, increasing the overall HRS signal. A higher resolving power also means that possible stellar effects, such as CLV and Doppler shadow, can be disentangled from the planet

signal more easily. However, for a certain R, the planet lines start to be resolved, above which the detection speed no longer increases. In reality, some wavelength regions will be richer in spectral features than others, depending on the type of planet. This influences the effect of λ_{span} on the detection speed.

In case B, the target spectrum consists of effectively one single, infinitely narrow line, e.g., exospheric helium, Hα. This requires only a very limited instantaneous wavelength coverage (as will also be the case for molecular oxygen in future reflected-light studies). In this case, the detection speed is proportional to

$$\Gamma_B \propto D^2 f R. \quad 2.$$

In case C, we consider high-contrast spectroscopy for which the residual seeing-halo of the host star is the dominant source of noise. Under such circumstances, the detection speed is proportional to

$$\Gamma_C \propto D^4 f \lambda_{span} R. \quad 3.$$

The detection speed depends on the telescope diameter D to the fourth power, because a change in D influences the size of the seeing disk in terms of angular resolution elements. In reality, however, the detection speed also critically depends on the performance of the AO system, the angular distance of the planet to the star in λ/D, and possible sky background and instrumental noise contributions.

Optical high-resolution spectrographs have almost exclusively been designed for RV measurements that require extreme wavelength stability at submeter-per-second precision over multiyear timescales. This is often achieved with a combination of light-scrambling, a fiber feed, *T–p* stability, and simultaneous wavelength calibration. Because atmospheric signals are generally too weak to measure planet RV at accuracies <100 m s^{-1}, such wavelength precision may be considered unnecessary. However, a very stable spectrograph with minimal instrumental artifacts does significantly help in removing telluric and systematic effects but may negatively affect its throughput.

Several teams are developing instrumentation specifically aimed at combining HRS with HCI, such as the Keck Planet Imager and Characteriser (KPIC) that combines starlight suppression using Keck's AO system and single-mode fibers transporting the light to the upgraded Near Infrared Spectrograph (NIRSpec) with a spectral resolving power of $R = 35{,}000$ (Mawet et al. 2016, Delorme et al. 2021). Similar instrument designs are chosen for VLT/HiRISE (High-Resolution Imaging and Spectroscopy of Exoplanets) (Vigan et al. 2024) and Ristretto (Chazelas et al. 2020), and Subaru/REACH (Rigorous Exoplanetary Atmosphere Characterization with High dispersion coronography) (Kotani et al. 2020). Interestingly, due to a reduced coupling in single-mode fibers, stellar flux is suppressed relative to that of the planet, a mechanism that is also utilized in the GRAVITY instrument at the VLT Interferometer (GRAVITY Collab. et al. 2020).

Table 1 shows high-resolution spectrographs that are currently most frequently used for exoplanet atmospheric observations and those that are in planning for the upcoming ELTs. **Figure 2** shows their detection speed for the different cases. Because Γ scales with D^{2-4}, the instruments on the largest telescopes are generally more powerful. Because optical high-resolution spectrographs have similar instantaneous wavelength coverages, spectrographs on 8–10-m-class telescopes are typically 4–6$\times$ faster than those on 4-m-class telescopes (1 transit on a larger telescope equals 4 to 6 transits on a smaller one). In the NIR wavelength regime, this is true for some instruments on smaller telescopes [such as CARMENES (Calar Alto high-Resolution search for M dwarfs with Exoearths with Near-infrared and optical Echelle Spectrographs), SPIRou (SPectropolarimètre InfraROUge), GIANO (the high-resolution near-IR spectrograph at Telescopio Nazionale Galileo) and NIRPS (Near Infra Red Planet Searcher)], which can partly compensate for this with their larger λ_{span} (case A) and high throughput.

Table 1 High-resolution spectrographs, currently most used or in planning[a]

Telescope (m)	Spectrograph (f, fiber; s, slit)	R	$\lambda_{min} - \lambda_{max}$	$\frac{\lambda_{span}}{\lambda}$	AO	Detection speed		
						A	B	C
Optical								
VLT (8.2)	ESPRESSO (f)	140k	0.38–0.79	0.70	n	**1**	**1**	–
	UVES (s)	100k	0.30–1.10	0.64	n	0.7	0.7	–
Keck (10)	HIRES (s)	70k	0.30–1.00	0.70	n	0.8	0.8	–
LBT (2 × 8.4)	PEPSI (f)	130k	0.38–0.91	0.30	n	0.8	2.0	–
Gemini (8.1)	MAROON-X (f)	80k	0.50–0.90	0.57	n	0.5	0.6	–
Subaru (8.2)	HDS (s)	45k	0.30–1.00	0.50	n	0.2	0.3	–
DCT (4.3)	EXPRES (f)	150k	0.38–0.68	0.57	n	0.2	0.3	–
ESO (3.6)	HARPS (f)	120k	0.38–0.69	0.58	n	0.1	0.2	–
CFHT (3.5)	ESPaDOnS (f)	81k	0.37–1.05	0.96	n	0.1	0.1	–
Calar A. (3.5)	CARMENES (f)	95k	0.52–0.96	0.59	n	0.1	0.1	–
TNG (3.6)	HARPS-N (f)	120k	0.38–0.68	0.58	n	0.1	0.2	–
ELT (39)	ANDES (f)	100k	0.40–1.00	0.86	y	20	16	449
GMT (25)	G-CLEF (f)	100k	0.35–0.90	0.88	n	9	7	–
Near-infrared								
VLT (8.2)	CRIRES+ (s)	100k	0.95–5.30	0.14	y	**1**	**1**	**1**
Keck (10)	NIRSpec (s)	35k	0.95–5.50	0.11	y	0.3	0.4	0.5
Gemini (8.1)	IGRINS (s)	45k	1.45–2.50	0.53	n	1.8	0.5	–
Calar A. (3.5)	CARMENES (f)	80k	0.96–1.71	0.56	n	0.6	0.2	–
ESO (3.6)	NIRPS (f)	82k	0.95–1.80	0.62	n	0.7	0.1	–
CFHT (3.5)	Spirou (f)	75k	0.95–2.35	0.85	n	0.9	0.1	–
TNG (3.6)	GIANO (f)	50k	0.90–2.50	0.94	n	0.7	0.1	–
ELT (39)	ANDES (f)	100k	1.00–1.80	0.57	y	100	25	2,264
TMT (30)	MODHIS (f)	100k	0.95–2.40	0.87	y	90	15	1,210
GMT (25)	GMTNIRS (f)	50k	1.07–2.45	0.78	y	37	6	340
Mid-infrared								
VLT (8.2)	CRIRES+ (s)	100k	0.95–5.30	0.14	y	**1**	**1**	**1**
Keck (10)	NIRSpec (s)	25k	0.95–5.50	0.11	y	0.3	0.4	0.5
ELT (39)	METIS (s)	100k	3.00–5.00	0.07	y	12	25	278
GMT (25)	GMTNIRS (f)	100k	2.90–5.30	0.59	y	36	9	336

Abbreviations: AO, adaptive optics; ESO, European Southern Observatory; n, no; NIR, near-infrared; y, yes; "–" indicates no data.

[a]Columns from left to right show the telescope, its primary mirror diameter, name of the spectrograph, entrance type, resolving power, wavelength regime, its instantaneous wavelength coverage expressed as λ_{span}/λ, and whether an AO system is present (y) or not (n). The last three columns show the detection speed relative to ESPRESSO and CRIRES+ on ESO's VLT for the different cases, assuming identical throughput and AO performance, as explained in the main text and presented in **Figure 2**.

The planned high-resolution spectrographs on future extremely large telescopes will be particularly powerful for case C, because the detection speed scales roughly with D^4, e.g., making METIS (Mid-Infrared E-ELT Imager and Spectrograph) on the Extremely Large Telescope (ELT) almost 300× faster than CRIRES+, and ANDES (ArmazoNes high Dispersion Echelle Spectrograph) at the ELT and MODHIS (Multi-Objective Diffraction-limited High-Resolution Infrared Spectrograph) on the TMT (Thirty Meter Telescope) faster by more than a thousand times. We note, however, that for the comparison of all these instruments it is assumed that throughput and AO performances are the same, which is challenging.

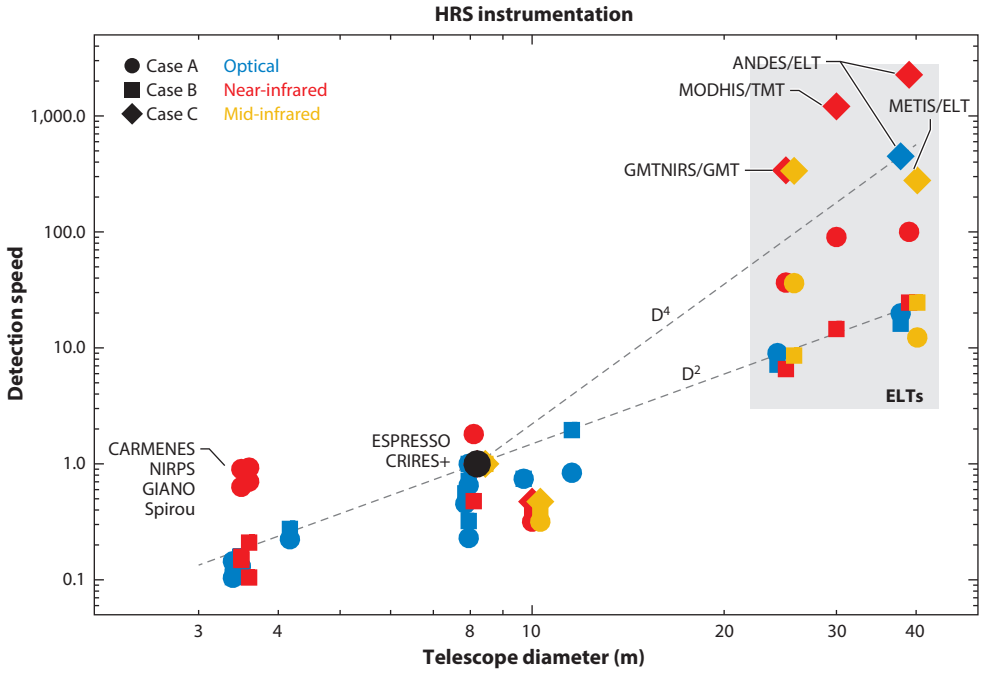

Figure 2

Detection speed of HRS observations for current and planned HRS instrumentation, normalized to the ESPRESSO (optical) and CRIRES+ (IR) spectrographs on the European Southern Observatory's Very Large Telescope. Three cases are specified (A, B, and C) as explained in the main text. ELT instrumentation will be up to three orders of magnitude faster than any instruments available now. Abbreviations: ANDES, ArmazoNes high Dispersion Echelle Spectrograph; CARMENES, Calar Alto high-Resolution search for M dwarfs with Exoearths with Near-infrared and optical Echelle Spectrographs; CRIRES, cryogenic high resolution IR Echelle Spectrometer; ELT, Extremely Large Telescope; ESPRESSO, Echelle SPectrograph for Rocky Exoplanets and Stable Spectroscopic Observations; GMT, Giant Magellan Telescope; GMTNIRS, GMT Near-IR Spectrograph; HRS, high-resolution spectroscopy; METIS, Mid-Infrared E-ELT Imager and Spectrograph; MODHIS, Multi-Object Diffraction-limited High-resolution Infrared Spectrograph; NIRPS, Near Infra Red Planet Searcher; Spirou, SPectropolarimètre InfraROUge; TMT, Thirty Meter Telescope; TNG, Telescopio Nazionale Galileo.

2.2. Observation and Data Analysis Strategies

Here, we explain how HRS observations are typically performed and discuss procedures for data analyses. For transmission and phase-curve observations, we review signal search techniques, and for the former we review how stellar surface effects like the Doppler shadow and CLVs can influence observations and need to be accounted for.

2.2.1. Transmission and phase-curve observations. A vital feature of time-differential HRS observations is their sensitivity to changes in Doppler shift of the planet spectrum as a function of orbital phase, as shown in **Figure 3**. The radial component of the planet orbital velocity can vary by tens of kilometers per second over a night's observations. Planet lines therefore rapidly change position relative to the much stronger stellar and telluric features. This means that the latter can be removed efficiently with a minimal impact on the planet signal. For this to work best, instrumental stability is key. Therefore, most observations consist of a continuous series of exposures, and possible calibrators are only invoked before and/or after the main observing sequence.

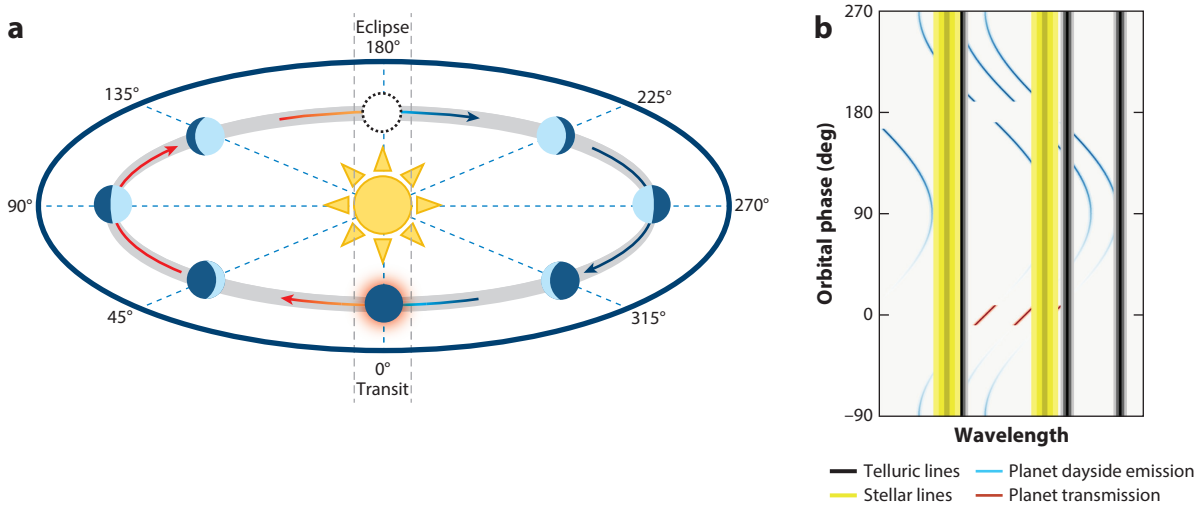

Figure 3

(*a*) Appearance of a planet as a function of orbital phase. If a planet is in a near edge-on orbit, the system will exhibit transits, allowing transmission spectroscopy, and eclipses when the planet is blocked from view. (*b*) In an observing sequence, telluric (*black*) and stellar (*yellow*) lines are quasi-static in wavelength, whereas those features originating from the planet (dayside emission in *blue*, transmission in *red*) exhibit strong Doppler effects.

Secondary eclipses are generally avoided because no exoplanet signal is present during these times, and planet-free spectra are often not needed for calibration purposes. HRS phase-curve observations are therefore also feasible for nontransiting planets.

When planning observations, one should avoid individual exposures that are too long such that planet signals get spectrally blurred; e.g., a planet in a circular 1-day orbit around a solar-type star has an orbital velocity of ∼200 km s^{-1}, with a change in the observed radial component of up to 1 km s^{-1} per minute. Up till now, most HRS transit and phase-curve observations are limited to hot Jupiters with fast-changing Doppler shifts; planets in wider orbits and/or around lower-mass stars have significantly lower orbital velocities, causing the change in Doppler shift to be insufficient to be utilized for telluric and spectral line removal. However, successful HRS phase-curve observations near quadrature, and transit measurements on relatively broad spectral features, indicate that HRS is also possible under these circumstances using other calibration methods, e.g., by comparing data taken during the transit with those taken outside the transit (Cheverall & Madhusudhan 2024) or spectra taken at very different phases.

2.2.1.1. Analysis of transmission and phase-curve data. The first important element of the data analysis of transmission and phase-curve data is the removal of the stellar and telluric contaminations. The telescope and instrument throughput generally varies with time and wavelength, e.g., due to seeing and airmass effects, which are impossible to calibrate accurately. To mitigate this, spectra are normalized and often high-pass filtered such that any broadband information is lost. To first order, the stellar lines do not vary in strength and position with time, meaning that removal of the mean spectrum takes care of the stellar contribution. Although the telluric line positions are quasi-stable with time, the line strengths vary owing to changes in air mass and possible changes in the observatory's atmospheric circumstances. To first order, these variations are similar for all tellurics and, therefore, can be measured in some strong lines and applied to all others. If needed, such correction can be performed for different telluric species, e.g., water and methane, separately.

For high S/n data, however, there are more subtle issues. The wavelength solution of the instrument may vary over time, or Earth-atmospheric winds may change the exact wavelength position of telluric lines. Seeing effects may change the spectral resolution for slit spectrographs. Stellar lines move owing to Earth's rotation and gravitational pull of the planet overnight, so lines may change in shape and strength owing to stellar activity. Instead of aiming to model all these different effects, a blind search for systematic effects in the data can be achieved using principle component analysis (PCA). Currently, one of the most popular algorithms is SysRem (Tamuz et al. 2005), which was originally developed to detrend light curves of transit surveys. SysRem and other algorithms that are being used to remove telluric and stellar contamination all affect and remove part of the target planet spectrum, and this is an effect that ideally needs to be taken into account, e.g., by analyzing artificial injection signals (see Section 2.4). In future analyses, it may be possible to simultaneously forward model and retrieve the stellar spectrum, telluric contamination, instrumental effects, and the planet spectrum without losses. Such an approach is already being implemented in high-contrast spectroscopy (Ruffio et al. 2019) for which the ratio of planet signal to the various noise contributions is significantly more favorable.

2.2.1.2. Cross-correlation, signal search techniques, and detection significance. The procedure to remove telluric and stellar features as described above largely preserves the line features in planetary spectra because of the change in Doppler shift of the planet over the observing sequence. Except for single-line analyses, the next step is to optimally combine the signals from different lines in the spectra, with each individual line still buried in the noise. This is often done by cross-correlating the residual spectra with a model template (for a detailed description, see the review by Birkby 2018). The more similar the model template is to the planet spectra, the higher the CC signals are. In the ideal case, the CC signal of a spectrum with N well-separated, equally strong lines will boost the S/n by a factor of $\sqrt{N}$ compared to that of one individual line. Alternative methods exist to extract the total planet signal, such as techniques using Doppler tomography (Watson et al. 2019, Matthews et al. 2024b) and log-likelihood methods that directly compare model templates with the data (Gibson et al. 2020).

In the case of direct fitting of template models to spectra, the change in planet Doppler shift as a function of time can be included as extra free parameters. Assuming circular orbits, and assuming that the orbital period and time of inferior conjunction are known, the RV of the planet depends on the RV amplitude, K_p, and the system velocity, V_{sys}, where the former is governed by the stellar mass and orbital inclination. In the case of combining CC signals, these are often calculated, Doppler shifted, and added, for a wide range of (K_p, V_{sys}) combinations to produce a so-called K_p–V_{sys} diagram. This has the added benefit of providing an independent estimate of the significance and reliability of any detected signal by showing the CC noise properties in regions of the K_p–V_{sys} diagram where no signal is expected (see Section 2.4). Note that atmospheric circulation patterns such as dayside-to-nightside winds may alter the exact K_p and V_{sys} of the planet signal. Noncircular orbits make the K_p–V_{sys} diagram less intuitive (e.g., Grasser et al. 2024).

The data points in a K_p–V_{sys} diagram are not independent from each other. **Figure 4*a*** shows a diagram for a noiseless time series of CC signals of a hypothetical hot Jupiter, and the corresponding K_p–V_{sys} diagram is shown in **Figure 4*b***. A signal from any single observation can in principle be fitted with a linear combination K_p and V_{sys}. For this reason, observations taken over a relatively short orbital phase range result in characteristic patterns as seen in **Figure 4*b***, with a typical X-shape if observations are combined from both before and after the secondary eclipse.

The K_p–V_{sys} diagram is often used to estimate the statistical significance and reliability of an observed signal by comparing it with the noise properties in this diagram away from the expected K_p and V_{sys}. One should be careful that the noise properties are a function of K_p, because the

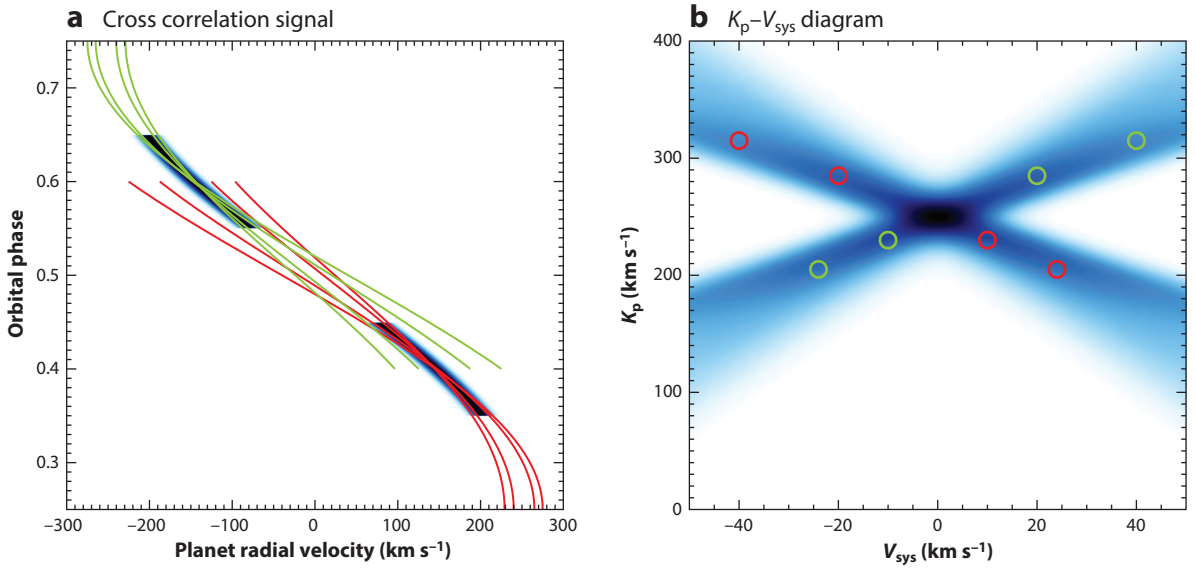

Figure 4

(*a*) A simulation of a cross-correlation signal (in *blue-black*) of a hot Jupiter observed over two orbital phase ranges, before ($\phi \sim 0.4$) and after ($\phi \sim 0.6$) secondary eclipse. (*b*) The resulting K_p–V_{sys} diagram with its characteristic X-shaped appearance. The origin of this X shape comes from the range of (K_p, V_{sys}) combinations that fit either the pre-eclipse or posteclipse part. This is shown by the red and green orbital solutions in panel *a*, which correspond to the (K_p, V_{sys}) combinations indicated by the red and green circles in the diagram in panel *b*.

lower the value of K_p, the smaller the change in RV during the observing sequence, and the more PCA algorithms will remove both the noise and any planet signal. For strong signals, aliasing may affect noise estimates. Alternatively, the Welch T-test can be used on the CC data by comparing the distribution of CC values inside and outside the expected RV trail (e.g., as shown in the left panel of **Figure 4**). One should take into account that neighboring CC values may not be independent of each other and that the properties of the CC noise may not be Gaussian, two basic assumptions of the Welch T-test.

HRS observers often make use of artificially injected signals. They can make sure that the different elements of the analysis pipeline work properly; they can help to assess the quality of the observed data throughout the night and/or over multiple nights and identify in which Echelle spectral orders specific molecules exhibit the strongest signals or where (residual) tellurics increase the local noise.

2.2.1.3. Rossiter–McLaughlin effect, Doppler shadow, and center-to-limb variations. In the case that HRS observers pursue a transmission spectrum with exoplanet atmospheric lines that are also present in the photosphere of its host star, the subsequent data analysis is prone to become significantly more complicated. Examples are alkali metals such as sodium in hot Jupiters and metal lines in UHJs ($T_{eff} > 2{,}000$ K). As a consequence, two effects may interfere with the planet transmission spectrum: the planet Doppler shadow and stellar CLVs.

The Doppler shadow is inherently the same as the RM effect and constitutes a temporal deformation of rotationally broadened stellar line profiles during transit. The occulted part of the stellar surface momentarily does not contribute to the overall stellar spectrum, leaving a shadow in the rotationally broadened lines. In the course of a transit, this shadow moves from the blue to the red wing of a stellar line, depending on the spin-orbit angle and the transit impact parameter.

The effective strength of the shadow depends on the opacity of the stellar line and the size of the planet. The Doppler shadow, which has a sign that is opposite to any exoplanet transmission signature, has to be modeled and removed from the data so as not to bias the results. In most systems, the transmission signal and Doppler shadow cross over in velocity at some point during transit. At such a moment in time, the effective size of the planet is larger owing to the additional absorption in its atmosphere, increasing the strength of the shadow and making it very hard to disentangle the two effects. Data from such an epoch are therefore often masked.

CLVs are also an important effect (Czesla et al. 2015, Yan et al. 2017). The local spectrum near the stellar limb is significantly different from that near the center of the stellar disk owing to the different angle of incidence. It means that near the beginning or end of a planet transit, the spectrum of the occulted stellar surface can be significantly different from the average spectrum and could be falsely attributed to a planet transmission signal.

In contrast to CLV, whose effects can be modeled and removed, other stellar surface inhomogeneities are more challenging. A planet's path over the stellar surface may cross more or fewer star spots; i.e., the occulted stellar surface may have on average a different effective temperature than the unocculted stellar surface. Such effects currently plague JWST transmission spectroscopy of planets around cool dwarf stars because we cannot differentiate between atmospheric transmission features and stellar surface effects (e.g., for water) (Moran et al. 2023). HRS observations could potentially help to distinguish between the two, because the RV of the occulted stellar surface is mostly different from that of the planet, although effects are small.

2.2.2. High-contrast spectroscopy. High-contrast HRS relies on a telescope with an AO system and optionally a coronagraph, from which light can be fed to a high-resolution spectrograph. Only in special cases, in which the planet is sufficiently far away from its host star, is no AO system required. In the case of planet thermal emission, the planet spectrum is in most cases significantly different from that of the star, because the effective temperature of the planet is much lower. In the case of scattered light, the planet and star spectrum are quasi-identical, but the reflected-light spectrum for the planet will be Doppler shifted for most orbital phases. Therefore, in both cases, planet light can be spatially as well as spectroscopically separated from that of the star, and many studies have identified HRS in combination with HCI as a potentially powerful method to find new planets and characterize them (e.g., Sparks & Ford 2002, Riaud & Schneider 2007, Kawahara & Hirano 2014, Snellen et al. 2015).

Blind searches for extrasolar planets with unknown positions require a form of integral field spectroscopy, which is currently only available at moderate spectral resolution [such as OSIRIS on the Keck Telescope, and ERIS (Enhanced Resolution Imager and Spectrograph) and MUSE (Multi Unit Spectroscopic Explorer) on the ESO's VLT]. In the case of a slit or fiber spectrograph, the planet position relative to that of the star must be known at the time of observation. If the host star is positioned on the detector and no coronagraph is present, exposure times are generally short to avoid saturation, meaning that the fainter planet spectrum could be degraded by instrumental read-out noise. By contrast the inclusion of a bright star spectrum can be beneficial for the data analysis.

The observed spectrum at the planet position generally contains flux from the star and planet, both modified by telluric absorption and possibly a sky background contribution. The latter can be effectively removed by moving the target along the slit or integral field unit (IFU) in between exposures. To first order, the stellar contribution (including tellurics) at the planet position only slowly varies with wavelength, allowing it to be scaled and removed or included in the forward modeling, with the observed star spectrum as a concurrent reference. The residual spectrum can subsequently be searched for planet molecular signatures using CC techniques as for transit and

phase-curve observations. However, obtaining a particularly high data quality requires more complex data analyses. For example, in the case of slit spectroscopy, a combination of good seeing and AO performance can cause the effective size of the star to be smaller than the slit width. This can cause the planet spectrum and associated telluric absorption to have a higher spectral resolution than the star spectrum with associated tellurics. Also, the wavelength solution may vary along the slit. Effective strategies for the removal of the stellar and telluric contributions need to take this into account and will depend on the particular atmospheric circumstances and planetary system; e.g., these can include radiative transfer modeling of telluric absorption and a set of principal components of the residuals to include systematic effects (Ruffio et al. 2023). Ideally, the stellar, planet, and telluric contributions should be simultaneously modeled with resolution effects to retrieve reliable and unbiased atmospheric parameters and their uncertainties, but this is beyond current methods and computer capabilities.

2.3. Atmospheric Modeling

Atmospheric modeling is an integral part of HRS observations. Model templates are used to tease out planetary signals, but they are also used for atmospheric retrieval studies. Any HRS observation can only be as good as the models used. Equally important is that any model is only as good as its underlying opacity data. Small errors in line positions can already lead to significant losses in signal. Therefore line positions need to be accurate to a fraction of the spectral resolving power. Another challenge is the line strengths, which become increasingly difficult to calculate and measure in laboratory settings at higher temperatures. Pressure broadening calculations may also be relevant, in particular for thermal emission spectra. Here, we discuss the origin of opacity data and common software packages for radiative transfer calculations, and we review the art of atmospheric retrievals.

2.3.1. Atomic and molecular opacity data. Accurate line data for atomic and ionic species are mostly readily available from databases such as from the National Institute of Standards and Technology (NIST; **https://www.nist.gov/pml/atomic-spectra-database**) and the Vienna Atomic Line Database (VALD; **https://vald.astro.uu.se/**). However, the spectra of polyatomic molecules are extremely complex with potentially up to billions of transitions playing a role. Although a proper discussion of the challenging practicalities of generating molecular line lists is beyond the scope of this review, this is a complex industry that deserves more attention. For example, it took a significant part of a quantum-chemistry Ph.D. project to calculate the line data for phosphine up to $T = 1{,}500$ K (Sousa-Silva et al. 2015). In addition to accurate line position, line broadening calculations can also be important for retrieval analyses.

A leading supplier of molecular line data at high temperatures is the ExoMol group, working with the concept of first principles theory informed by experiment (Tennyson & Yurchenko 2021). ExoMol now validates and adjusts line energies depending on laboratory measurements, leading to very high-accuracy line lists. Its database contains line lists for more than 80 molecules, often including isotopic variants. High-temperature line lists have also been produced by the TheoRets (Theoretical Reims–Tomsk Spectral) project (Rey et al. 2016), MoLLIST (Molecular Line Lists, Intensities and Spectra) (Bernath 2020), and by NASA Ames. The HITRAN (High-Resolution Transmission Molecular Absorption) database (Gordon et al. 2017) provides line data applicable at low temperatures for several dozens of small molecules present in the Earth atmosphere, and this is expanded to higher temperatures in HITEMP (the high-temperature molecular spectroscopic database) (Hargreaves et al. 2020). If the line data are insufficiently accurate or incomplete, it can significantly hamper the detection of molecules, as shown by Hoeijmakers et al. (2015) for the case of TiO and de Regt et al. (2022) for VO. The optical spectra of both these molecules are

particularly challenging as they are dominated by electronic transitions, but significantly improved line data have become available from McKemmish et al. (2019) and Bowesman et al. (2024).

2.3.2. Radiative transfer calculations. Radiation transfer calculations are needed to produce model exoplanet emission and transmission spectra. An example of an easy-to-use publicly available python package for this purpose is `petitRADTRANS` (Mollière et al. 2019), but there are many alternatives such as `HELIOS` (Malik et al. 2017), `EXo-REM` (Baudino et al. 2015), `NEMESIS` (Irwin et al. 2008), `HyDRA` (Gandhi & Madhusudhan 2018), `CHIMERA` (Line et al. 2014), `PLATON` (Zhang et al. 2019), and others. These codes typically require precomputed opacity grids of relevant atoms, ions, and/or molecules as functions of pressure and temperature, in addition to continuum opacity sources such as H_2–H_2 and H_2–He collision-induced absorption and H^-. Most radiative transfer codes also have a way to include the effects of clouds, either physically motivated (e.g., $MgSiO_3$, Fe, etc.) or simple gray cloud models, controlled by parameters such as the atmospheric pressure and opacity at the cloud base, and a power law index that sets the decay toward lower pressures.

For the calculation of transmission spectra, in its basic form, the planet atmospheric structure is assumed to be independent of longitude or latitude, and the assumed T–p profile and surface gravity (e.g., at 1 bar) is converted to a radius–temperature relation and parameterized as a set of layers, each with a specific pressure and temperature. The optical depth for a ray of light grazing the atmosphere is determined as a function of impact parameter and subsequently converted into a transmission spectrum. For the calculation of planet emission spectra, similar setups are used for calculating the transmission of each layer, using a range of angles between the direction of the light rays and the atmospheric normal to determine the average emission from the planet disk. Because the full radiative transfer solution in a scattering atmosphere is computationally slow, it is often assumed that the scattering is weak compared to the absorption.

2.3.3. Retrievals of atmospheric parameters. The aim of atmospheric retrievals is to determine atmospheric properties and their uncertainties from an observed spectrum. In the context of exoplanets, this was first pioneered by Madhusudhan & Seager (2009), forward modeling millions of (low-resolution) spectra for a ten-dimensional grid of input parameters. Subsequently, for all these model spectra it was determined whether they, within uncertainties, fit the observed data to derive the atmospheric properties.

Atmospheric retrievals for HRS are challenging for several reasons. In the case of HRS transit and phase-curve spectroscopy the observed spectrum is modified by the data reduction processes, such as PCA and filtering techniques. The forward models need to go through similar data processing to allow for a reliable comparison with the data. Furthermore, HRS data volumes can be enormous with up to tens of thousands of pixels per individual spectrum. Brogi & Line (2019) presented a Bayesian atmospheric retrieval framework applicable to HRS observations, for which they developed a mapping from CC to log-likelihood. Gibson et al. (2020) subsequently introduced a framework that directly computes the likelihood of a model fit to observations. Monte Carlo Markov Chain (MCMC) and nested sampling techniques can then be employed to explore parameter space. Fisher et al. (2020) have presented a random forest supervised machine learning technique to perform the retrievals. Ruffio et al. (2019) pioneered an approach in which the signal is forward modeled in such a way that preprocessing of the data (such as CC and data interpolation) is minimized, preserving the statistical properties of the data as much as possible and therefore the likelihood accuracy.

A key aspect of atmospheric retrievals is the choice of assumptions for chemical modeling and parameterization of the atmospheric temperature structure. When chemical equilibrium is assumed, chemical abundances vary as a function of altitude and strictly depend on temperature, pressure, metallicity, and atomic ratios such as C/O, whereas disequilibrium processes such as

photochemistry or rain-out condensation are ignored. Because vertical mixing timescales can be significantly shorter than those to reach chemical equilibrium, in particular at low pressures, a quench pressure can be introduced (Zahnle & Marley 2014). Below this pressure, higher up in the atmosphere, the chemical abundances are assumed to be governed by chemical equilibrium at the quench pressure because vertical mixing dominates. For example, in some hot Jupiters the temperature at millibar pressures is low enough that significant methane would form if the atmosphere would be in chemical equilibrium. However, the gas largely originates from deeper atmospheric layers with higher temperatures and does not have time to adjust to the local circumstances (Cooper & Showman 2006). An alternative assumption is to adopt free chemistry without any restrictions on volume mixing ratios except that they are constant as a function of altitude. The abundance of every absorber is then a free, independent parameter. If the quality of the data allows, it can be very informative to compare outcomes of different retrieval setups to address the validity of chosen assumptions.

Also the atmospheric T–p profile can be parameterized in many ways, from a complete free format to largely physics-informed T–p profiles (e.g., Guillot 2010). A choice must also be made whether to include clouds (physically motivated or gray) in the retrievals or not. If an opaque cloud layer is present, but clouds are not included in the retrieval setup, the retrieved T–p profile may become deformed. For example, because in such a case no flux is coming from below the cloud layer, this can be mimicked by an isothermal profile (Burningham et al. 2017).

2.4. Potential Pitfalls

HRS can be a very complex technique, in terms of both observations and data analysis. Here, a nonexhaustive list of potential pitfalls is discussed for those HRS users new in the field.

1. **Exposure time blending:** When planning transit or phase-curve spectroscopic observations, individual exposure times should not be set too long to avoid spectral blending. The change in the RV of the planet may be so large during the exposure that it affects the effective resolving power of the observations.
2. **Overlap of transmission signal with Doppler shadow:** For some transiting systems, the trail of the Doppler shadow largely overlaps with that of the planet transmission signal. This means that at any moment during transit, the radial component of the orbital velocity of the planet matches the RV of the occulted stellar surface, making analyses of planet transmission features that are also present in the stellar photosphere very challenging. Notable examples are HD 209458b and MASCARA 1b.
3. **Velocity broadening of scattered light signals:** When probing starlight reflected off atmospheres of short-period planets, one has to take into consideration that reflected signals can be significantly velocity broadened (e.g., Spring et al. 2022). Although the spin-velocity of the host star may be very slow, in the rest frame of the planet it completes about one revolution per orbital period, making detection of scattered light more challenging. Because in the Tau Boötis system both star and planet are tidally locked, the scattered stellar lines are unbroadened and expected to be significantly more narrow than those in the direct stellar spectrum, making it a popular target for reflected-light studies (Charbonneau et al. 1999, Collier Cameron et al. 1999, Hoeijmakers et al. 2018b); however, the planet turned out to be very dark.
4. **Conversion of signal-to-noise to statistical significance:** The S/n ratio of a measurement can be converted into a statistical significance by assuming a Gaussian noise distribution. Because in this case a signal at $S/n = 3$ corresponds to a 0.3% probability that it is caused by a random noise fluctuation, this could in principle be considered a firm

detection. However, the fact that many post processing choices have been made to arrive at such a detection—how to extract the spectra and remove the telluric and stellar absorption lines, which spectral model to choose to perform the CC, and freedom in the exact location of the signal in the (K_p, V_{sys}) diagram due to a priori unknown atmospheric winds effects—should not be overlooked. Also, overall it can be difficult to assess to what extent the noise distribution is indeed Gaussian. These effects make the probability that a spurious signal is seen at $S/n = 3$ significantly higher than 0.3%. Therefore, many studies use a threshold of $S/n = 4$ or 5 to claim a detection, which still may not be sufficient. Even more conservative is to require a detection in multiple transits or phase-curve observations.

5. **Accidental fabrication of fake signals:** For many HRS measurements, data over multiple nights and/or many spectral orders have to be combined. This is often done by deriving the CC functions per order and night, which are subsequently combined using optimal weights. These weights can be important because the data quality may be different from one night to the next, and a specific molecule may only have significant opacity in certain spectral orders of the spectrograph. It is of upmost importance that the calculation of these weights is based purely on injected signals and not on the observed data. Otherwise the analysis may result in a fake, fabricated signal (for a discussion, see Cabot et al. 2019). A modern high-dispersion spectrograph, for example, can have 80 spectral orders. If there is no planetary signal at all, and the resulting CCs from the individual orders contain all pure uncorrelated Gaussian noise, still ∼16% and ∼2.5% of the orders will exhibit a 1σ and 2σ CC-peak, respectively, which with optimal weights will combine into a completely spurious signal of $\sim 6\sigma$. Note that the contribution from the signal injection to the CC function needs to be separated from that of the observed spectrum; otherwise the latter is still prone to bias the determination of the optimal weights (Cheverall et al. 2023).

   Also, the number of PCA or SysRem components, required to remove the telluric and stellar features in the spectra, needs to be chosen, which may also depend on the observing night and spectral order (e.g., depending on the strength of the telluric features). These need to be treated in the same way.

6. **Unrealistic and biased uncertainties in retrieved parameters:** Results from atmospheric retrieval analyses are mostly not free from biases and can provide unrealistically small uncertainties. There can be several reasons for this that are important to investigate. Different datasets, i.e., with different wavelength regimes, spectroscopic resolving power, or S/n levels, can result in retrieval results that are significantly different from each other. First of all, it is generally assumed that spectral data points and their uncertainties are independent of each other, which is often not the case, e.g., due to model inaccuracies or errors in telluric removal. The atmospheric temperature structure (and abundance profiles) can be parameterized in many ways, with possibly none providing the perfect solution and, therefore, all resulting in their own biases. One way to characterize the strength and scale length of correlated noise is by using Gaussian processes and including them in the retrieval setup (Kawahara et al. 2022). In addition, uncertainties from preprocessing are mostly not included, such as small errors in the flux calibration from a spectroscopic standard star that result in inaccuracies in the spectral slope. These can be included by adding extra order-normalization parameters or spectral slope parameters, or by removing any low-frequency spectral information (by high-pass filtering) altogether.

   Another important source of unrealistically small uncertainties is the inclusion of too few free parameters in the retrievals. The Bayesian information criterion (BIC) is widely used to assess whether extra parameters provide a significantly better fit. If not, such extra parameters are not included in the retrieval. However, even if extra parameters do not result in a

better fit, they may still influence the uncertainty (and best-fit value) of other parameters. For example, for an observed spectrum with relatively low S/n, retrievals may suggest that there is no statistical evidence for any deviation from chemical equilibrium or for the presence of clouds. However, performing a retrieval with free-chemistry and inclusion of the possibility of clouds, or 3D effects, can significantly change the outcome and enlarge the uncertainties on retrieved abundances. Sometimes strict assumptions are chosen, because the data would otherwise not provide meaningful constraints.

3. RESULTS ON CLOSE-IN EXOPLANETS

In this section, literature results on HRS atmospheric characterization of close-in exoplanets, mostly hot Jupiters, are summarized and discussed. In such a vibrant field of research as exoplanet characterization it is impossible to provide a complete overview of all the work presented in the literature, in particular because during writing new studies appeared on an almost daily basis. We review observations of specific atmospheric species, constraints on temperature structure, atmospheric dynamics and outflows, reflected-light searches, and chromatic Doppler-shadow measurements.

3.1. Measurements of Atoms, Ions, and Molecules

In this subsection, measurements of atoms, ions, and molecules are discussed. First, results on the sodium H and K lines are summarized, followed by those on other metals and ions, and carbon monoxide, water, and other molecules.

3.1.1. Sodium H and K lines. Sodium was predicted to produce the strongest features in optical transmission spectra of hot Jupiters (Seager & Sasselov 2000) and was the first chemical element detected in an exoplanet atmosphere, in HD 209458b using the HST (Charbonneau et al. 2002). Studying sodium in transmission is challenging because stellar sodium lines are very strong, in particular for G- and K-type stars. This means that the S/n of a planetary sodium signal at mid-transit is generally low, and Doppler shadow and CLV effects are particularly strong. Although Snellen et al. (2008) confirmed the original HST detection of sodium with the Subaru, Casasayas-Barris et al. (2021) find no evidence for sodium at this level in superior ESPRESSO (Echelle SPectrograph for Rocky Exoplanets and Stable Spectroscopic Observations) results taken more than a decade later. For this system, the RV trail of the planet almost overlaps with the Doppler shadow, making the analysis of this target particularly difficult. In the earlier studies, CLV effects were not taken into account, so at least part of the original sodium signal could be attributed to this. However, due to the overlap of the RV trail and Doppler shadow, the RM effect at sodium wavelengths is stronger in the case of a planetary atmospheric contribution, counteracting a transmission signal (see Carteret et al. 2024 for a recent discussion). Alternatively, long-term variability (i.e., due to changes in cloud coverage in the terminator region) could play a role, although temporal variability can too easily be invoked to explain differences between datasets.

Figure 5*a* provides an overview of the currently known population of transiting hot Jupiters around bright stars ($V < 13.5$) available in the NASA Exoplanet Archive (retrieved on April 1, 2024, from **https://exoplanetarchive.ipac.caltech.edu**). Plotted are their equilibrium temperature, $T_{\rm eq}$, versus what we define as the scale height contrast (SHC). The latter is the expected transmission signal from an opaque atmospheric ring with a thickness of one scale height, H, corresponding to

$$SHC = (2\pi R_{\rm p} H)/(\pi R_{\rm s}^2),$$

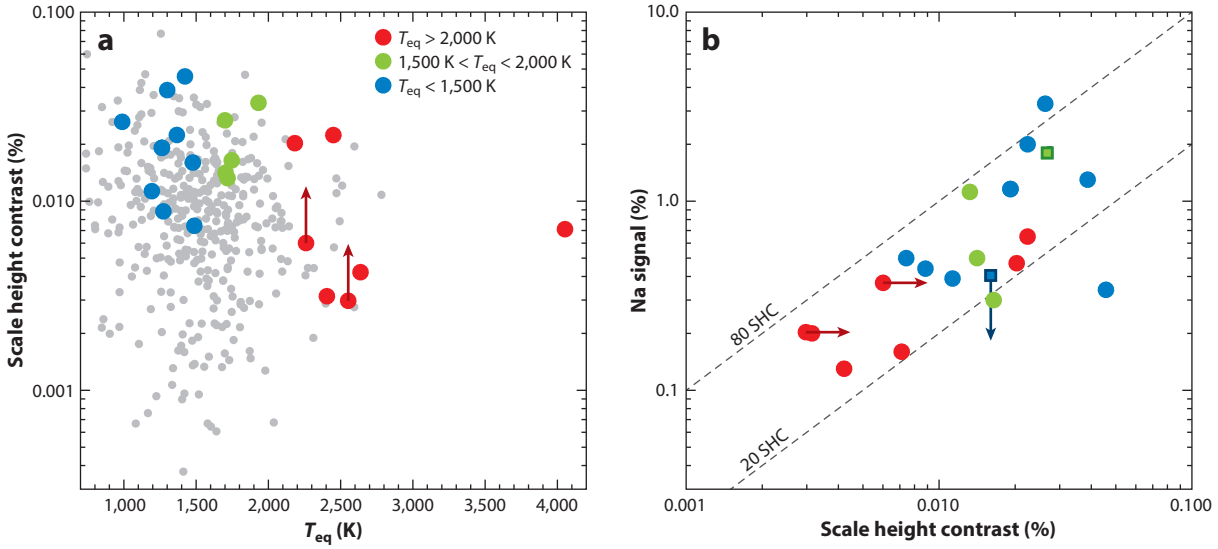

Figure 5

(*a*) Currently known population of transiting hot Jupiters around bright stars with orbital periods of <10 days, masses >0.1 M_{Jup}, and radii >0.5 R_{Jup}. Their equilibrium temperatures (assuming a zero Bond albedo) are plotted versus SHC, which is the expected transmission signal from an opaque atmospheric ring with a thickness of one scale height. The colored symbols (*red*: T_{eq} > 2,000 K; *green*: 1, 500 K < T_{eq} < 2,000 K; *blue*: T_{eq} < 1,500 K) are planets with HRS sodium detections presented in the literature. Those with lower limits in their scale height contrast have an unknown mass. The signals of the two planets (HD 209458b and WASP-17b) marked with squared symbols are derived from their integrated light curve, assuming the sodium signal is 0.5 Å wide. (*b*) Strength of the sodium signal versus scale height contrast. Data taken from Bello-Arufe et al. (2022, 2023), Langeveld et al. (2022), Snellen et al. (2008), Mounzer et al. (2022), Casasayas-Barris et al. (2019), Zhang et al. (2022), Žák et al. (2022), Seidel et al. (2022, 2023b), Wyttenbach et al. (2017), Zhou et al. (2012), Chen et al. (2020b), and Rahmati et al. (2022) and are provided in **Supplemental Table 1**. Abbreviations: HRS, high-resolution spectroscopy; SHC, scale height contrast.

where R_p and R_s are the planet and host star radius, respectively. It is a first-order measure of how strong a transmission signal is expected to be. The thick circles indicate those hot Jupiters that have an HRS sodium detection presented in the literature, where the color is an indication of T_{eq}. HRS detections exist for hot Jupiters with a wide range of equilibrium temperatures, up to the hottest planets known. This literature sample of planets with sodium detections is likely marred with biases. Also, nondetections and their associated upper limits are poorly reported and are not included here. The SHC of those planets with detections is larger than average, probably because mostly promising targets are being observed, and those with a smaller SHC fall below typical detection limits.

Figure 5*b* shows the observed strength of the sodium signals versus SHC. The data, and their origin from the literature, are presented in **Supplemental Table 1**. This strength is simply taken as the relative depth of the transmission signal, ignoring spectral resolution and the intrinsic width of the sodium features. Despite the many caveats regarding sample selection, completeness, and other biases, it is interesting to see that the strengths of the sodium signals correlate with SHC. A similar analysis was performed by Langeveld et al. (2022), who showed a comparable relationship on a smaller sample. The sodium signals in hot Jupiters extend typically between 20 and 80 scale heights above their continuum absorption. A notable exception is WASP-127b, which has the largest SHC in the sample but a relatively weak sodium feature (Allart et al. 2020). Assuming that these sodium features dominantly originate from the hydrostatic part of hot Jupiter atmospheres, the observed planet-to-planet variations could be driven by variations in high-altitude

cloud decks, sodium abundance, velocity broadening, and photoionization for planets at the highest temperatures. Alternatively, one could argue that many of the signals are so strong, associated with microbar pressure levels, that they likely originate from exospheric outflows (Seidel et al. 2020).

3.1.2. Other metals and ions. Because sodium is so prominent in the optical transmission spectrum of hot Jupiters, it is the subject of many studies. In particular in UHJs, numerous other metals and ions have been detected. Seager & Sasselov (2000) already showed that potassium should also provide observable transmission signals for hot Jupiters. However, observational successes have been limited. Although some popular high-resolution spectrographs do not cover the potassium lines, they are at wavelengths hampered by telluric absorption from molecular oxygen. Initial reports of potassium from HST observations (Sing et al. 2015) of WASP-31b have not been confirmed with HRS (Gibson et al. 2019). Chen et al. (2020b) reports the only HRS potassium detection, in WASP-52b.

At temperatures $T_{eq} > 2{,}000$ K, optical transmission spectra of gas giant planets are expected to be cloud free, close to chemical equilibrium, and dominated by features from atomic and ionized metals (Kitzmann et al. 2018). Indeed, HRS has been prolific in detecting such signals in UHJs (Hoeijmakers et al. 2018a, 2019). **Figure 6** shows a schematic overview of detections presented in the literature so far in the context of the periodic table, in either neutral or ionized state, including alkali metals (e.g., lithium, sodium, potassium), alkaline earth metals (e.g., magnesium, calcium, strontium, and barium), and transition metals (e.g., scandium, titanium, vanadium, chromium, manganese, iron, cobalt, nickel, yttrium).

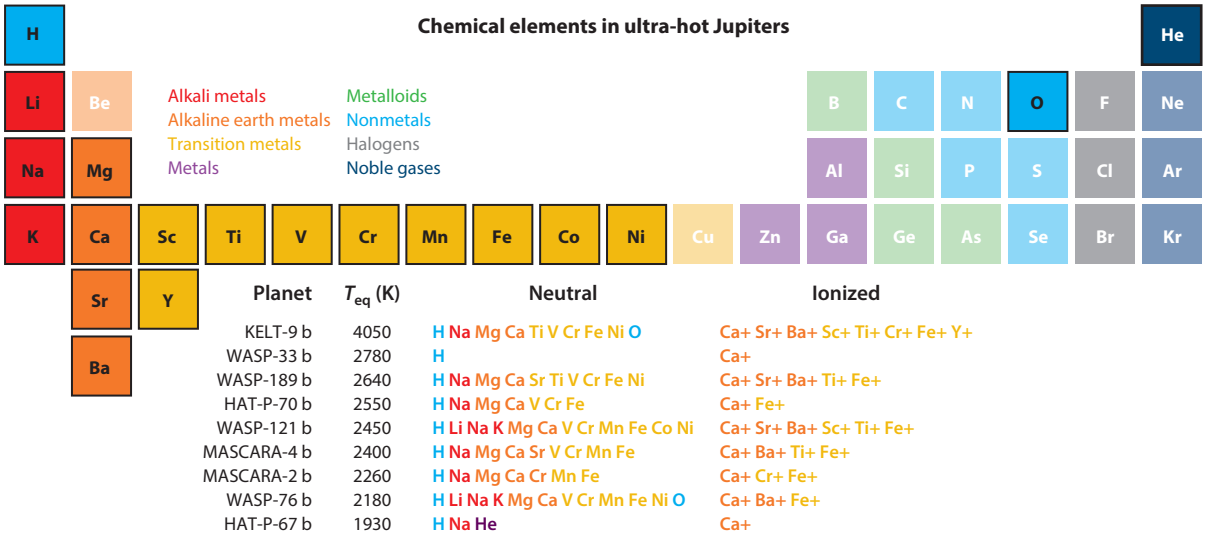

Figure 6

Overview of the chemical elements detected in the transmission spectra of UHJs. Planets are ordered by decreasing equilibrium temperature. WASP-33b is a more challenging target due to the presence of significant stellar pulsations. Data taken from Borsa et al. (2021b), Borsato et al. (2023), Hoeijmakers et al. (2018a, 2019, 2020, 2022), Yan & Henning (2018), Cauley et al. (2021), Yan et al. (2019), Prinoth et al. (2023, 2024a), Stangret et al. (2020, 2022), Bello-Arufe et al. (2022, 2023), Azevedo Silva et al. (2022), Ben-Yami et al. (2020), Merritt et al. (2021), Maguire et al. (2023), Gandhi et al. (2023b), Jiang et al. (2023), Zhang et al. (2022), Casasayas-Barris et al. (2019), Fossati et al. (2023), Nugroho et al. (2020b), Ehrenreich et al. (2020), Tabernero et al. (2021), Deibert et al. (2021), and Pelletier et al. (2023). Abbreviation: UHJs, ultra-hot Jupiters.

It is interesting to discuss those elements that are not seen. Most of these have cosmological abundances that are too low, are insufficiently spectroscopically active, or have no significant lines in the optical wavelength regime (e.g., Kesseli et al. 2022). Also, condensation on the nightside can play a role, where those elements with a high condensation temperature (refractory elements such as Ti, Al, and Sc) could rain-out on the nightside and be cold-trapped deep in the atmosphere, preventing them from being mixed back into the upper layers, resulting in low abundances in both dayside and transmission spectra (Hoeijmakers et al. 2022, Pelletier et al. 2023). Titanium is indeed not detected in the three studied UHJs with the lowest equilibrium temperature (**Figure 6**). At lower temperatures, it is expected that iron will rain out (Kitzmann et al. 2018, Ehrenreich et al. 2020). This is in agreement with nondetections of iron and nickel in HAT-P-67b in contrast to sodium and ionized calcium (Bello-Arufe et al. 2023).

Ionization may also play a role in the apparent underabundance or nondetections of neutral species (Kesseli et al. 2022, Gandhi et al. 2023b). Some metalloids and nonmetals have been detected in dayside spectra (Cont et al. 2022a) or locked up in molecules (such as CO) (Yan et al. 2023). Detections of chemicals with very high atomic mass have been reported, such as rubidium and samarium (Jiang et al. 2023) in MASCARA-4b and terbium in KELT-9b (Borsato et al. 2023). These species have very low cosmic abundances, and their presence in UHJ atmospheres needs confirmation.

In recent years, great advances have been made in retrieval studies of exoplanet atmospheres such that abundances can be quantified. UHJs are ideal targets for this purpose owing to the expected chemical equilibrium and absence of clouds. Relative chemical abundances are generally much better constrained by transmission spectra than absolute abundances because they are less sensitive to the atmospheric temperature structure and absolute pressures probed. Gibson et al. (2022) retrieves relative abundances for WASP-121b consistent with solar values, except magnesium. For WASP-76b, Pelletier et al. (2023) show seven species to have abundances relative to iron similar to protosolar (except for those elements that are cold trapped), whereas its overall metallicity appears only possibly slightly enriched (at $\sim 1\sigma$) compared to its host star. Gandhi et al. (2023b), in a homogeneous study, retrieves the absolute and relative abundances from the optical transmission spectra of six UHJs. They show that iron abundances agree well with solar values but that other species exhibit more variations for reasons discussed above. Note that these retrieval studies assume the atmospheres to be in hydrostatic equilibrium, whereas some species may be associated with exospheric outflows (Zhang et al. 2022).

3.1.3. Carbon monoxide, water, and other molecules. The first overtone absorption band of CO at 2.3 μm is an ideal target for ground-based HRS, due to its strong, well-separated set of lines in a relatively telluric-free part of the spectrum. Detections of CO and H_2O have historically dominated the HRS literature, which is shown to be present in both the transmission and dayside spectra of the two archetype hot Jupiters HD 209458b (Snellen et al. 2010, Brogi et al. 2017, Hawker et al. 2018) and HD 189733b (Birkby et al. 2013, de Kok et al. 2013, Rodler et al. 2013, Brogi et al. 2016). These molecular gases have so far not been widely studied in transmission spectra (Maimone et al. 2022, Boucher et al. 2023, Basilicata et al. 2024, Hood et al. 2024), which is in contrast to thermal dayside spectra, where they are found in relatively cool planets, such as HD 189733b and 51 Pegasib, to UHJs (e.g., Birkby et al. 2017, Holmberg & Madhusudhan 2022, Brogi et al. 2023). In the case of nontransiting planets, detection of CO and/or H_2O have led to the determination of their orbital inclinations, breaking the $\sin i$ degeneracy and solving for their planetary masses (Brogi et al. 2012, 2013, 2014; Rodler et al. 2012, Guilluy et al. 2019), which is a unique ability afforded by HRS.

Assuming that, in atmospheres at $T > 1{,}000$ K, carbon and oxygen atoms are primarily locked up in CO and H_2O (ignoring CH_4 that can become abundant in carbon-rich atmospheres),

atmospheric retrieval analyses can constrain the C/O ratios, which Öberg et al. (2011, 2023) propose can shed light on planetary formation processes (Öberg et al. 2011, 2023). However, care must by taken in comparing results between different planets, because different assumptions in the retrieval setups (such as free chemistry, chemical equilibrium, or the presence of clouds) may bias the results. One could argue that the fact that most results are close to the solar C/O value (0.55) indicates that HRS atmospheric retrieval analyses are rather reliable. Interestingly, some C/O ratios derived from JWST observations deviate significantly from that of solar (i.e., C/O $\sim$ 0.1 for HD 209458b) (Xue et al. 2024). Ramkumar et al. (2023) find a C/O ratio consistent with solar for the UHJ MASCARA-1b, as do Line et al. (2021) for WASP-77Ab (C/O = 0.59$\pm$0.08), while Bazinet et al. (2024) find a slightly elevated value for HIP 65Ab. Brogi et al. (2023) and Lesjak et al. (2023) derive C/O values consistent with 0.75 for WASP-18b and WASP-43b, respectively, whereas the nondetection of H_2O in Tau Boötis b points to a C/O $>$ 0.6 (Pelletier et al. 2021). However, by accounting for undetectable oxygen due to thermal dissociation, Brogi et al. (2023) derive C/O $<$0.34.

Molecules other than CO and H_2O are more rarely detected with HRS. The hydroxyl radical OH, which is the expected photodissociation product of H_2O, was first found in the dayside spectrum of the UHJ WASP-33b (Nugroho et al. 2021) and confirmed by Cont et al. (2022b). Landman et al. (2021) detect OH in the transmission spectrum of WASP-76b, confirmed by Cheverall et al. (2023). Retrieval analysis of WASP-33b by Finnerty et al. (2023) implies that OH is significantly more abundant than H_2O, suggesting the latter is almost completely photodissociated and showing how general assumptions on chemical and physical atmospheric processes can strongly bias retrieved C/O ratios. HCN is detected in the transmission spectrum of HD 189733b (Cabot et al. 2019) and HD 209458b (Hawker et al. 2018, Giacobbe et al. 2021) and tentatively in WASP-76b (Sánchez-López et al. 2022a).

Metal hydrides and oxides are very prominent in the spectra of late M dwarfs and brown dwarfs and could therefore also be expected to be present in the atmospheres of irradiated gas giants. For example, titanium-oxide (TiO) and vanadium-oxide (VO) have been proposed as high-altitude absorbers that cause thermal inversion layers (Fortney et al. 2008). However, detection of such molecules has been problematic owing to suboptimal line lists (Hoeijmakers et al. 2015, de Regt et al. 2022) and possibly because they are cold trapped on the nightside of hot Jupiters (e.g., Parmentier et al. 2013). The quest for TiO in the dayside spectrum of WASP-33b serves as an example of how elusive observational evidence for hydrides and oxides have been. TiO was first detected by Nugroho et al. (2017). An attempt to confirm this detection with an improved line list using the same dataset provided no conclusive evidence (Herman et al. 2020, Serindag et al. 2021). Cont et al. (2021) provide some evidence for TiO, whereas Yang et al. (2024) report a nondetection. Reports of detections and nondetections seem to come and go, although Prinoth et al. (2023) claim a 6.6σ TiO detection in the transmission spectrum of WASP-189b. Pelletier et al. (2023) present an exciting detection of VO, whereas Flagg et al. (2023) find evidence for CrH. The most extensive search for a metal hydride, FeH, involved transmission spectra of twelve planets; Kesseli et al. (2020) find no signals, corresponding to abundance upper limits of $<10^{-7}$ for most planets. As FeH is a powerful surface-gravity indicator, it is not seen in the spectra of red giant stars. Because transmission spectroscopy probes low atmospheric pressures like those for the photospheres of red giants, it may only be present deeper in the atmosphere.

Species CH_4, NH_3, and C_2H_2, have so far only been claimed to be detected using a 4-m-class telescope (Guilluy et al. 2019, Giacobbe et al. 2021, Basilicata et al. 2024). However, such detections have been met with skepticism, because the combined detections of these molecules are difficult to explain chemically, and some are expected to be significantly less abundant than

CO and H_2O in hot Jupiter atmospheres. Indeed some of these measurements have recently been refuted (Blain et al. 2024).

3.2. Atmospheric Temperature Structure

HRS phase-curve spectroscopy is a very powerful tool to constrain the atmospheric temperature structure of extrasolar planets. Theoretical considerations and early spectroscopy with *Spitzer* (e.g., Burrows et al. 2007, Fortney et al. 2008, Knutson et al. 2008) initiated a discussion about the possible prevalence of thermal inversion layers within the photospheres of hot Jupiters. Such inversions are present in most Solar System planets (albeit not all in their photospheres). The power of HRS comes from the fact that in the case of a thermal inversion individual lines are seen in emission, which turned out not to be the case for most hot Jupiters (e.g., Schwarz et al. 2015).

Figure 7 shows the current results from HRS dayside spectroscopy. Seventeen hot Jupiters and UHJs have detections from H_2O, CO, and/or iron. All observed hot Jupiters show absorption lines and have noninverted photospheres, whereas all observed UHJs (T_{eq} > 2,000 K) exhibit emission lines and have thermal inversions. For a thermal inversion to be present, stellar radiation needs to be absorbed at high altitude. This is most likely caused by species that are efficient absorbers at wavelengths in which the host star radiates most of its energy, i.e., the UV/optical wavelength regime. Although metal oxides, in particular TiO and VO, have been proposed to play this role, they appear not to be prominent absorbers in hot Jupiters and UHJs. Although sodium absorbs in the optical, it is not present specifically at T_{eq} > 2,000 K. It has therefore been proposed that iron and other metals, which characteristically are spectroscopically active in the photospheres of UHJs, may be driving the inversions (e.g., Lothringer & Barman 2019, Yan et al. 2020).

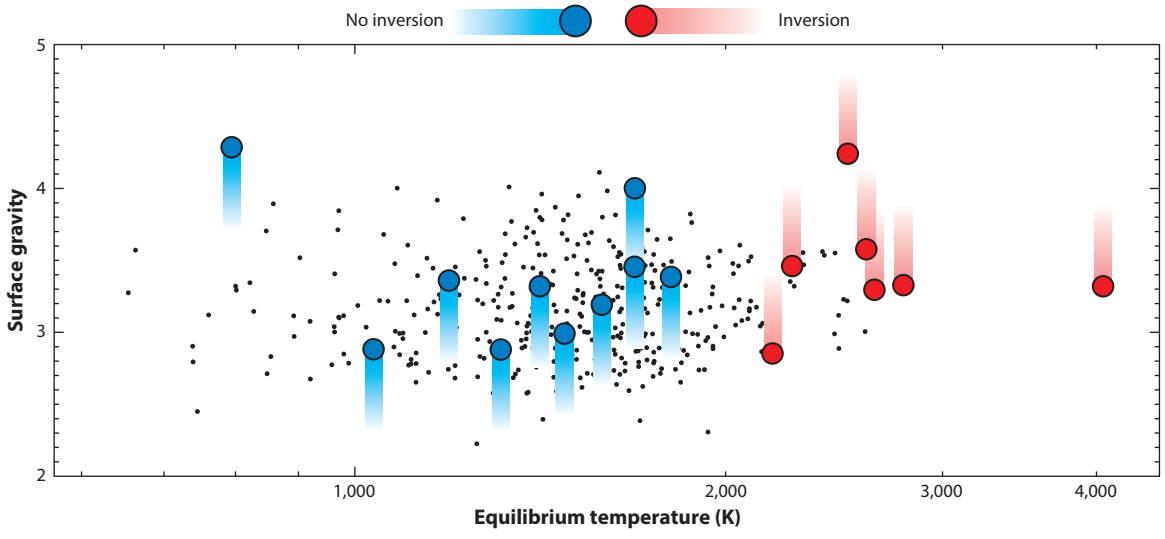

Figure 7

Exoplanets with atomic or molecular detections in their dayside spectra, showing either absorption lines, indicative of noninverted atmospheres (*blue symbols*), or emission lines, implying thermal inversions (*red symbols*). A clear dichotomy is visible at $T_{eq} \approx 2{,}000$ K. For nontransiting planets, a radius of 1.25 R_{Jup} was assumed. The black dots indicate the general population of transiting gas giants as in **Figure 5**. Data taken from Pino et al. (2020), Guilluy et al. (2019), Piskorz et al. (2018), Bazinet et al. (2024), Brogi et al. (2023), Ramkumar et al. (2023), Brogi et al. (2012, 2013, 2014), Brogi & Line (2019), de Kok et al. (2013), Yan et al. (2020, 2022a,b, 2023), Birkby et al. (2013, 2017), and Line et al. (2021).

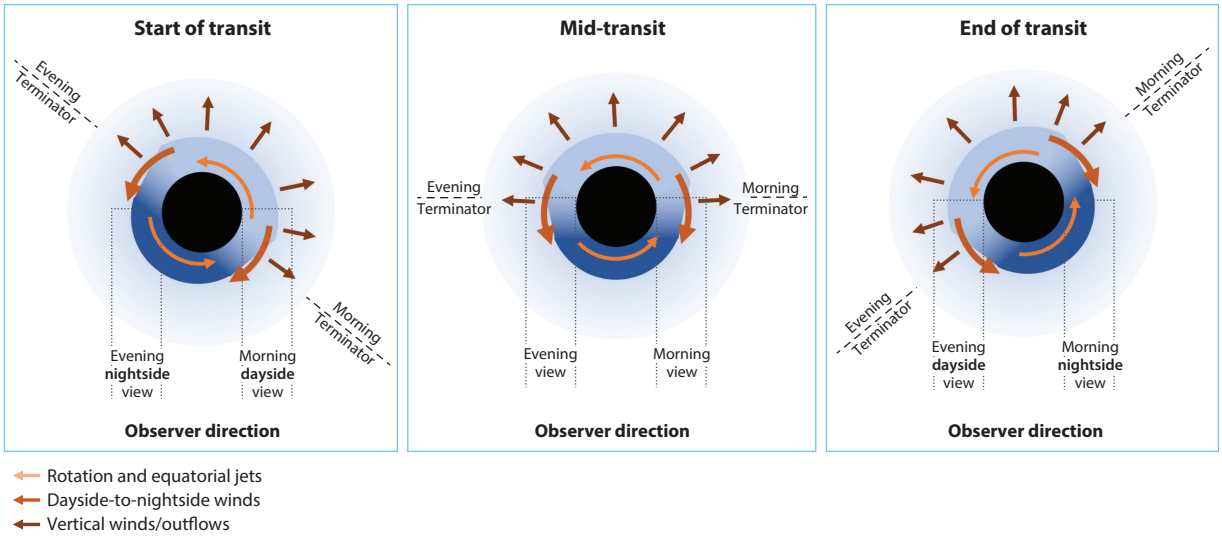

Figure 8

Schematic representation of different dynamical effects probed by transmission HRS, with the planet moving from left to right over the stellar surface. These include planet rotation and equatorial jets, dayside-to-nightside winds, and outflows leading to atmospheric loss. The viewing angle on the terminator region changes during transit. In the first part of the transit, the nightside and dayside of the evening and morning limb are probed, respectively, and vice versa at the end of the transit. Abbreviation: HRS, high-resolution spectroscopy.

3.3. Atmospheric Dynamics, Rotation, and Outflows

Brown (2001) already advocated more than two decades ago that HRS would be a powerful tool to study atmospheric dynamics. It is indeed an area of research that is unique to this type of observation. The short-period planets that are probed today through transmission and phase-curve spectroscopy are expected to be tidally locked, implying that they should have equatorial spin velocities in the range of 1–10 km s^{-1}, which is accessible through line broadening (e.g., Brogi et al. 2016). In addition, the planetary rotation and strong stellar irradiation are expected to drive complex atmospheric dynamics. Three-dimensional global circulation models, also including effects like magnetic drag, are developed to capture such effects and link them to state-of-the-art HRS observations (e.g., Showman et al. 2008, 2013; Rauscher & Menou 2010; Parmentier et al. 2013; Kempton et al. 2014; Beltz et al. 2022). **Figure 8** illustrates the different effects to which HRS is potentially sensitive. Planetary rotation with strong stellar forcing is expected to induce equatorial jets that amplify line broadening. Global dayside-to-nightside winds may transport heat from the dayside to the nightside, which blueshifts transmission lines. In addition, strong stellar irradiation may induce vertical Parker-type winds, leading to outflows and atmospheric loss. For the most extreme close-in planets (in terms of a/R_*), the orientation of the planet changes significantly during transit, meaning that different parts of the evening and morning limbs can be studied, resulting in fascinating effects (Ehrenreich et al. 2020).

3.3.1. Dayside-to-nightside winds. Winds that travel from the dayside to the nightside result in a global blueshift of transmission lines. Their velocities are thought to result from a balance between the day/night temperature difference and dissipation mechanisms (e.g., Miller-Ricci Kempton & Rauscher 2012). The first evidence of such winds, although at low significance, was presented by Snellen et al. (2010) using CO transmission lines in HD 209458b.

Before conclusions can be drawn from Doppler-shifted measurements of transmission lines, it must be realized that several effects can influence such observations. The orbital ephemeris needs to be well constrained. For a planet in a two-day orbit around a solar-type star, a 1-min error in transit-timing results in a 0.4 km s^{-1} error in the expected RV of the planet, whereas an error in eccentricity of 0.01 can change the planet's expected velocity during transit by 1 km s^{-1}. Also, the system velocity can be difficult to determine for a fast-rotating star. The stellar gravitational redshift (0.6 km s^{-1} for our Sun) needs to be taken into account, as well as does the possible blueshift due to convection cells. If elemental transitions are used that are also present in the stellar atmosphere, such as sodium or iron, an imperfect correction for the Doppler shadow and/or CLV effects may also affect wind measurements.

Reports of dayside-to-nightside winds have been rather scattered so far, mostly focusing on a single elemental species or molecule for a single planet. Uncertainties are difficult to assess, with different studies of the same planet, even using the same species, sometimes resulting in significantly different wind speeds. Pai Asnodkar et al. (2022) show that even variability may play a role, with four measurements of iron in the transmission spectrum of KELT-9b taken at different epochs resulting in blueshifts ranging from 4 to 11 km s^{-1}. There have only been a few systematic studies of wind effects in exoplanet atmospheres. Notably, Langeveld et al. (2022) studied ten hot Jupiters and UHJs in sodium to find blueshifts up to 5 km s^{-1}, but all bar one was within 2σ from zero—hence, they were barely significant. The retrieval study by Gandhi et al. (2023b) of six UHJs show them all to have a net blueshift, from <1 km s^{-1} for MASCARA-2b to 7 km s^{-1} for WASP-76b, mostly at higher statistical significances.

Figure 9 attempts to reveal a pattern in the very heterogeneous and incomplete data on atmospheric winds, based on different atmospheric species. Warm and fluffy planets possibly

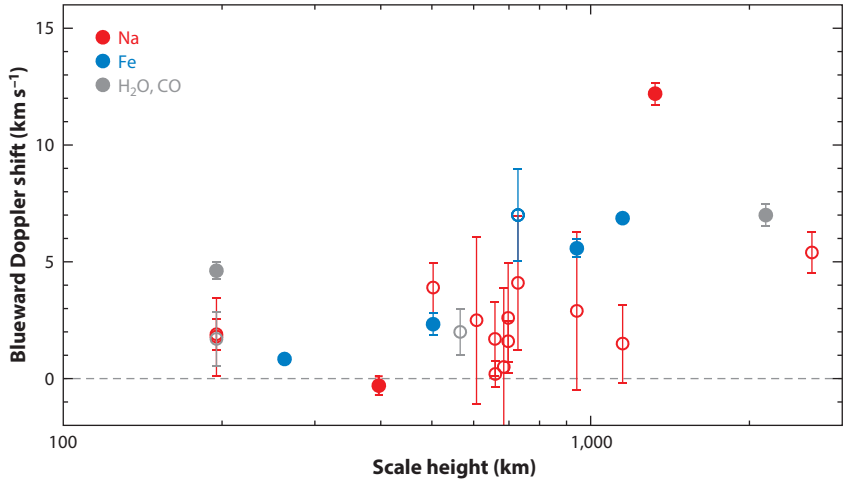

Figure 9

Dayside-to-nightside winds, as derived from Doppler shifts in transmission spectra as a function of atmospheric scale height. Data points in red, blue, and gray are based on Na, Fe, and H_2O, CO, respectively, and open circles indicate their uncertainties are >1 km s^{-1}. Although this is a very heterogeneous and incomplete sample, those planets with larger scale heights appear to have, on average, larger dayside-to-nightside winds. Data taken from Langeveld et al. (2022), Gandhi et al. (2023b), Pai Asnodkar et al. (2022), Boucher et al. (2021, 2023), Louden & Wheatley (2015), Brogi et al. (2016), Snellen et al. (2010), Mounzer et al. (2022), Seidel et al. (2023b), Chen et al. (2020a), Wyttenbach et al. (2017), and Rahmati et al. (2022).

exhibit stronger winds: All planets with measured winds >5 km s^{-1} have atmospheric scale heights >700 km.

3.3.2. Rotation, equatorial jets and time-resolved spectroscopy. Although dayside-to-nightside winds are expected to dominate at low pressures high-up in hot Jupiter atmospheres, most heat transport from the dayside to nightside is predicted to come from equatorial jets deeper in the atmosphere. Indeed, space-based thermal phase-curve observations of hot Jupiters often show (e.g., Knutson et al. 2007) that their hottest parts are significantly offset from a planet's substellar point. HRS observations can directly probe these equatorial jets through line broadening in addition to what is expected from bulk rotation of a tidally locked planet (e.g., Louden & Wheatley 2015, Brogi et al. 2016). However, different contributions from the leading and trailing limbs, and contributions from the dayside-to-nightside winds, thermal broadening, and possible residuals from the RM effect, can significantly complicate such analyses. It is therefore very helpful to add extra information using time-resolved transit spectroscopy. Contributions from the leading (morning side) and trailing (evening side) limbs can be isolated by focusing on the ingress and egress transmission spectrum, respectively. In this way, Louden & Wheatley (2015) derive wind velocities on the leading and trailing limbs of HD 189733b that are consistent with predictions from atmospheric circulation models and can be understood as a combination of tidally locked planetary rotation and an eastward equatorial jet. Seidel et al. (2020, 2021) retrieved wind patterns, speeds, and temperature profiles from the line shape of the sodium doublet of the UHJ WASP-76b, showing that this is best fit with a uniform dayside-to-nightside wind and a significant vertical wind (see Section 3.3.3). More recently, these researchers used the unprecedented collecting area of the four VLT telescopes combined with ESPRESSO's 4UT mode to probe the sodium line in the UHJ WASP-121b (Seidel et al. 2023a) and identify a high-velocity component during egress interpreted as an equatorial dayside-to-nightside wind across the evening limb.

Ehrenreich et al. (2020) realized that for planets in particularly close-in orbits, i.e., with small a/R_* (ratio of orbital distance to stellar radius), the orientation of the planet also changes significantly during transit. Due to this Ehrenreich Effect, the viewing angle of WASP-76b varies by about 30° from ingress to egress (see **Figure 8**). It means that early on in the transit, the transmission spectrum probes on the morning limb on the atmospheric dayside of the planet and on the evening limb on the nightside. Late in the transit this is reversed, and the dayside evening limb and nightside morning limb are probed, respectively. Because contributions from both limbs can be separated owing to their different Doppler shifts (due to planet rotation), the planet atmosphere can be traced from dayside to nightside on the evening and morning side. For WASP-76b, Ehrenreich et al. (2020) show that this results in a transmission signal in iron that increases significantly in strength and blueshift during transit (observation confirmed by Kesseli & Snellen 2021), interpreted as due to a lack of iron on the morning-nightside due to rain-out. Wardenier et al. (2021) show using 3D Monte Carlo radiative transfer modeling that the signal could also be caused by a substantial temperature asymmetry. Gandhi et al. (2022) separately conducted an atmospheric retrieval analysis for the morning and evening terminator regions, finding evidence for both a lower iron abundance and lower temperature at the morning limb.

Although WASP-76b is the optimal target to probe the Ehrenreich Effect (among all studied UHHs), and iron the optimal species, similar effects have been detected for other metals and other planets (e.g., Bourrier et al. 2020, Hoeijmakers et al. 2020, Stangret et al. 2020, Kesseli et al. 2022). In addition to time-resolved transmission spectroscopy, emission spectroscopy can also provide information about heat circulation in combination with global circulation models (e.g., Pino et al. 2022, van Sluijs et al. 2023).

3.3.3. Outflows and atmospheric loss. In the years after the first detection of an exoplanet atmosphere (Charbonneau et al. 2002), the archetypal transiting planets HD 209458b and HD 189733b were shown to exhibit Lyα absorption at levels of a few percent during transit (Vidal-Madjar et al. 2003, Lecavelier Des Etangs et al. 2010), caused by a significant halo of exospheric hydrogen. The warm Neptune GJ 436b was found to have such a halo extending as a cometary tail around the planet, causing a 50% transit depth (Ehrenreich et al. 2015). Unfortunately, probing hydrogen through Lyα is challenging owing to geocoronal absorption, which blocks all potential signals near zero velocity, and absorption by the interstellar medium beyond the Local Bubble (30–100 pc). Transmission signals by hydrogen from higher energy levels, such as Hα (Yan & Henning 2018), other Balmer lines (Wyttenbach et al. 2020, Yan et al. 2021), and even Paschen-beta (Sánchez-López et al. 2022b), are accessible with HRS and point to exospheric gas associated with atmospheric escape but seem restricted to planets with the highest temperatures (Zhang et al. 2022).

The seminal work by Seager & Sasselov (2000) predicted the presence of helium absorption at 1,083 nm in the transmission spectra of hot Jupiters. After some failed attempts to detect this transition, it was overlooked for almost two decades until interest was rejuvenated by Oklopčić & Hirata (2018) and subsequently observed with HST (Spake et al. 2018) as a direct probe of atmospheric loss. Because it is in a wavelength region relatively free of telluric absorption, ground-based HRS has proven to be a very powerful technique to probe its spatial and dynamical structure (Allart et al. 2018, Nortmann et al. 2018). This has revolutionized the study of atmospheric escape, although interpretation of the 1,083-nm helium line and conversion to atmospheric losses is less straightforward than that for Lyα. The helium line originates from an excited metastable 2^3S state for which the population is governed by the radiation field of the host star: Although extreme-UV flux ionizes the helium ground state, mid-UV flux ionizes the metastable state (Oklopčić 2019). Close-in planets around K stars are expected to show the strongest helium absorption, whereas those orbiting early-type stars, despite probably having high mass-loss rates, may show no signal because the metastable state is not sufficiently populated (e.g., KELT-9b) (Nortmann et al. 2018).

About a dozen planets have been detected in HeI, some at very high S/n. Both of the warm Saturns WASP-69b and WASP-107b, located near the edge of the evaporation desert, are shown to have strong absorption signatures with blueshifts of several kilometers per second and post-transit absorption pointing to comet-like tails (Nortmann et al. 2018, Allart et al. 2019). For the latter it is estimated that its extended thermosphere fills half of the Roche lobe with an estimated escape rate of metastable helium of 10^6 g s^{-1} (Allart et al. 2019). Recently, the cometary tail of WASP-69b was found to extend to 7.5 planetary radii behind the planet (Tyler et al. 2024). Helium absorption signals can be significantly more extended and complex than this. HAT-P-67b is exhibiting helium absorption in a large leading trail up to 130 planetary radii (necessarily observed over multiple nights) (Gully-Santiago et al. 2024). Giant tidal tails of escaping helium have been found both leading and trailing the hot Jupiter HAT-P-32b (Zhang et al. 2023b), which spans a projected length over 53 planetary radii. It is the intricate interplay among orbital shear, dayside and nightside mass-loss asymmetries, and confinement by the stellar wind that is expected to determine the spatial and dynamical morphology of exospheric helium (McCann et al. 2019). By the absence of any stellar wind, atmospheric loss from the planet dayside and nightside will cause a leading and trailing tail, respectively, due to orbital shear. A strong stellar wind will push any material into a cometary tail behind the planet. Zhang et al. (2020) suggest that the 1,083-nm helium line may also be observed as airglow emission away from transit but that this may require one of the upcoming extremely large telescopes. Helium studies have also been extended to mini-Neptunes (e.g., Zhang et al. 2023).

3.4. Reflected-Light Searches

The field of exoplanet atmospheric characterization started with attempts to use ground-based HRS observations to probe reflected light, i.e., starlight scattered by planet atmospheres (e.g., Collier Cameron et al. 1999, Charbonneau et al. 1999). Unfortunately, progress in this particular avenue has been very difficult ever since. Although scattered light signals could in principle be as high as $\sim 10^{-4}$ for highly reflective (i.e., cloudy) atmospheres, hot Jupiters turn out to have very low geometric albedos. Many studies have focused on the Tau Boötis system (Charbonneau et al. 1999, Leigh et al. 2003, Hoeijmakers et al. 2018b) because both star and planet are tidally locked. This means that the star is stationary in the planet rest frame, canceling out the velocity broadening in the reflected-light spectrum and maximizing a potential atmospheric signal (see also Spring et al. 2022).

Martins et al. (2015) provided evidence for a reflected-light signal from 51 Pegb, pointing to a planet radius of 1.9 R_{Jup} and a high geometric albedo of 0.5. However, subsequent studies have not been able to confirm the signal (Spring et al. 2022). It is possible that HRS reflected-light detections will need to wait for the future ELTs. In particular, the combination of HRS with HCI probing neighboring stars will be orders of magnitudes more sensitive to scattered light signals and will be able to probe a new regime of cooler planets that are expected to have significantly higher geometric albedos than hot Jupiters (Lovis et al. 2017).

3.5. Chromatic Doppler-Shadow Measurements

Originally proposed two decades ago (Snellen 2004, Dreizler et al. 2009), the RM effect or Doppler shadow can in principle also be used to probe exoplanet atmospheres. At wavelengths in which the effective planet size (due to extra atmospheric absorption) is larger, the amplitude of the RM effect and Doppler shadow will also be larger. In measuring the amplitude of the RM effect as a function of wavelength, a transmission spectrum can be constructed. In this way, Di Gloria et al. (2015) reconstructed the broadband transmission spectrum of HD 189733b, showing evidence, albeit at low significance, for a Rayleigh scattering slope similar to that found using HST (Sing et al. 2011) data. Independent observations and analyses reflect comparable conclusions (Cristo et al. 2022). For HD 209458b, a remarkable similarity was found between the broadband RM transit spectrum and that from HST by Santos et al. (2020). Borsa et al. (2019, 2021a) found chromatic RM effects for UHJs but do not present transmission spectra.

Analysis of the chromatic Doppler shadow remains highly challenging. Although based on shape deformations of stellar lines, these same lines may also be present in the planet transmission spectrum (as in the case of sodium, or any metal lines in the case of UHJs), highly complicating the analysis. Depending on the orbital configuration (i.e., spin-orbital alignment) and intrinsic properties of a planet's atmospheric absorption, the strength of the Doppler shadow may significantly vary during transit. This is most apparent when the planetary absorption and Doppler shadow overlap in velocity. These specific epochs are often left out of transmission spectroscopic analyses. However, with the limited lifetime of HST, the chromatic Doppler shadow or RM effect may at some point be the only way to obtain information on blue-optical broadband transmission spectra in the near future.

4. RESULTS ON WIDE-SEPARATION EXOPLANETS

Compared to HRS transit and phase-curve measurements, HRS combined with HCI is still in its relative infancy. First observations of this type were performed at medium spectral resolution, such as the important work by Konopacky et al. (2013), whereas Snellen et al. (2014) showed its potential by measuring the radial orbital velocity and $v \sin i$ of the super-Jupiter Beta Pictoris b.

In this section, I highlight some of the state-of-the-art observations, focusing on the first results from KPIC (Keck Planet Imager and Characterizer) on Keck, and CRIRES+.

The larger the angular distance between planet and host star, the more accurately the planet spectrum can be separated from that of the star. In many cases, the high-resolution spectra that are obtained with this technique are of significantly better quality than transmission or phase-curve spectra. In this section, some recent results are also included from isolated brown dwarfs for which the spectra reach S/n ratios of >50 per spectral resolution element. In addition to providing potential insights into different formation pathways for brown dwarfs and planets, such observations serve as ideal benchmarks to test the accuracy and robustness of analysis techniques and to gauge the level of detail that can be retrieved in the case of future high-quality exoplanet spectra.

4.1. Molecular Abundances and Atmospheric Temperature Structure

In the past 2–3 years, HRS studies of directly imaged planets and brown dwarfs have not only resulted in detections of many molecular species but also in stringent constraints on abundances and T–p profiles. About two dozen substellar objects have now been targeted with HRS at high S/n, allowing reliable retrieval of atmospheric parameters. We are at the start of a wave of many such investigations that so far have mainly targeted atmospheres in K band, where H_2O and CO are the two dominant contributors for hot or warm objects >1,500 K, with an increasing contribution from CH_4 and NH_3 toward lower temperatures (e.g., Wang et al. 2021, Xuan et al. 2022, Costes et al. 2024, de Regt et al. 2024). The hotter targets also show clear absorption by hydrogen fluoride (HF) and several atomic species such as sodium, calcium, and titanium (González Picos et al. 2024).

Figure 10 shows an overview of a heterogeneous sample of young and older field brown dwarfs and super-Jupiters for which metallicities and C/O ratios have been measured. Because these objects are significantly more massive than Jupiter (10–50 M_{Jup}), it may not be surprising that their metallicities are broadly consistent with that of our Sun, except for Beta Pictoris b and HD 984b,

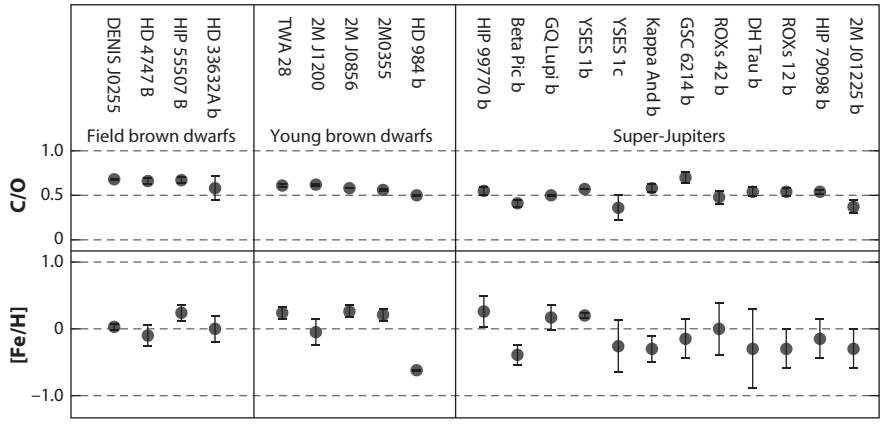

Figure 10

High-resolution spectroscopy atmospheric retrieval results on C/O ratio and metallicity (derived from C/H) as present in the literature, for field brown dwarfs, young brown dwarfs, and super-Jupiters. For some measurements, the error bars are smaller than the symbol sizes. Data taken from de Regt et al. (2024), González Picos et al. (2024), Zhang et al. (2024b), Landman et al. (2024), Zhang et al. (2021), Xuan et al. (2024a), Costes et al. (2024), Wang et al. (2021), Xuan et al. (2022), Xuan et al. (2024b), Bryan et al. (2018), 2020b), and Hsu et al. (2024) and provided in **Supplemental Table 2**.

Supplemental Material >

which appear to have a lower metal content (Costes et al. 2024, Landman et al. 2024). The metallicities of the super-Jupiters seem on average somewhat lower than those of the brown dwarfs, but this is unlikely to be statistically significant. They have generally lower-quality spectra, resulting in larger error bars and therefore may be biased. Also, the well-known log(g)-metallicity correlation adds to the uncertainty. Although C/O ratios could potentially provide insights in their formation processes, almost all objects are consistently measured to be within the C/O = 0.5–0.65 range.

As a detailed case study, the work by de Regt et al. (2024) is discussed, who obtained a K-band spectrum of the $T = 1{,}400$ K field brown dwarf DENIS J0255-4700 at a S/n of 40 per resolution element as part of the CRIRES+ SupJup Survey. They compared atmospheric retrievals using three different set-ups: (*a*) free chemistry, in which the abundances of relevant chemicals are constant with pressure but otherwise unconstrained; (*b*) equilibrium chemistry, in which the chemical abundances at each pressure are set by the metallicity, C/O ratio, and temperature; and (*c*) quenched equilibrium chemistry, in which the abundance follows chemical equilibrium down to a certain pressure, below which the abundances are forced to be constant. The physical idea is that below this quench pressure (so, higher up in the atmosphere), the vertical mixing timescales are shorter than the chemical timescales such that the chemical abundances are governed by the circumstances at the quench pressure. Interestingly, the high data quality allows distinctions to be made between these scenarios. The free chemistry and quench-pressure setup result in a very similar solution in T–p profile, chemical abundances, and C/O ratio. The unquenched chemical equilibrium model provides a significantly worse fit, resulting in a different metallicity and C/O ratio. Basically, the relatively small methane signal pushes the chemical equilibrium model to higher temperatures. At lower S/n, one may have chosen a model with the lowest number of parameters (i.e., following the BIC), which is the chemical equilibrium model, possibly skewing the retrieved parameters. In more extreme cases, the lack of methane, though it is expected at the derived atmospheric temperatures, points to quenching (e.g., Zhang et al. 2024b).

Atmospheric retrieval setups also allow for the introduction of clouds, either gray or physically motivated (e.g., $MgSiO_3$, Fe, etc.). However, so far, most retrieval analyses find little evidence for significant cloud opacity. Finding evidence for clouds is generally challenging for HRS observations over a relatively narrow wavelength range, where slight changes in the temperature structure can mimic clouds. Most analyses have so far been performed in K band, which probes relatively high altitudes, and clouds may be present below the photosphere (Xuan et al. 2022). J- and H-band HRS spectra should be significantly more sensitive to cloud layers. As shown by de Regt et al. (2024), the K-band spectrum of DENIS J0255 provides no statistical evidence for cloud opacity, but the cloud-free model-flux at J band is a factor of ∼3 higher than measured by 2MASS (Two-Micron All Sky Survey) photometry, meaning that clouds indeed need to be present but possibly below the K-band photosphere.

High S/n spectra also allow detailed modeling of the temperature structure, e.g., by parametrizing the T–p profile with temperature gradients (Zhang et al. 2023a) to retrieve the radiative–convective boundary (Marley & Robinson 2015), as is done for GQ Lupi b (González Picos et al. 2025). In addition, the retrieval of a slight deviation from the adiabatic temperature gradient at high pressure suggests the presence of nonadiabatic convection or the cloud–T–p degeneracy (e.g., Tremblin et al. 2019). An additional effect that has been identified in high S/n spectra is veiling (Folha & Emerson 1999). Some young substellar objects may have a circumplanetary disk that significantly contributes to the observed spectrum as a continuum source, making the object spectral lines appear shallower. For example, significant veiling at ∼14% of the continuum flux at K band is measured for the young brown dwarf 2M J1200 (González Picos et al. 2024), and it is found to be very prominent in the K-band spectrum of the GQ Lupi host star at >50% levels (González Picos et al. 2025).

The higher the data quality, the more complex the modeling needs to be to appropriately fit the data. Although K-band HRS monitoring of the nearby brown dwarf Luhman 16b resulted in the first brown dwarf Doppler-imaging map (Crossfield 2014), de Regt and colleagues (S. de Regt, I. Snellen, D. Gonzáles Picos, P. Molliere, manuscript in preparation) show that at $S/n \geq$ 100/pixel, HRS becomes sensitive to spatial inhomogeneities. This can reveal the presence of cloud bands and vortices in single-epoch observations by deviation from the expected rotational line-broadening profile from a homogeneous limb-darkened disk. Other model refinements are possibly required at the highest levels of data quality, such as molecular abundance variations with altitude due to non–local thermodynamic equilibrium processes.

4.2. Orbital and Rotational Dynamics

The atmospheric retrieval analyses as discussed above also provide the projected rotational broadening, or $v \sin i$, of the observed targets. Although $\sin i$ is unknown for most objects, for a randomly oriented sample, the true spin velocity is on average only 15% higher. Also, only 15% of a sample of randomly oriented targets is expected to have $i < 30°$ with true spin velocities that are larger by a factor of two or more than the measured $v \sin i$. In principle, their inclinations can be determined if they show significant flux variability that lead to the derivation of their spin period. In combination with constraints on their orbital inclination, the radial component of the obliquity can be determined, as shown by Bryan et al. (2020a), who derive a planetary obliquity for the super-Jupiter 2M J0122b of at least 49^{+27}_{-21} degrees.

Investigating the rotation rates of exoplanets may shed light on their formation mechanisms, how their angular moment is set via interaction with a circumplanetary disk through magnetic coupling, and possibly altered later through collisions or gravitational tides (Bryan et al. 2018, 2020b). For those substellar objects with measured $v \sin i$, the radii can be estimated from their derived surface brightness, flux density, and distance to Earth. **Figure 11** shows the measured $v \sin i$ as a function of radius for field brown dwarfs, young brown dwarfs, and super-Jupiters. In any evolutionary sequence it would be expected that the youngest, bloated objects rotate the slowest, subsequently cool and contract over time, and spin up. Although this is a very heterogeneous sample, all objects with $R > 1.75$ R_{Jup} bar one have a $v \sin i < 10$ km s^{-1}, whereas most targets with $R < 1.75$ R_{Jup} exhibit significantly higher spin velocities. In the future, large and complete samples of brown dwarfs and gas-giant exoplanets for which the ages, radii, and masses can be derived more accurately, will provide interesting constraints on the evolution of angular momentum of these objects. Although the current sample is a varied assortment, and the uncertainties in radii are large, the distribution of $v \sin i$ for Jupiter-sized objects seems to have a larger spread than expected from a random distribution in $\sin i$ alone. Objects of the same size seem to have significantly different rotation velocities.

In addition to rotational broadening, atmospheric retrievals also reveal the RV of the exoplanet, and if that of the host star is determined, the radial component of its orbital velocity. This can be used to constrain the planet orbital elements, as shown by Schwarz et al. (2016) for GQ Lupi b. There is growing evidence that some super-Jupiters at wide orbits have high eccentricities that point to a formation in a close-in orbit and subsequent planet–planet interactions (e.g., Dupuy et al. 2023).

4.3. Isotope Measurements

The ability to detect individual isotopologues and determine isotope ratios in exoplanet atmospheres opens up a new pathway to constrain planet formation and evolutionary processes (e.g., Mollière & Snellen 2019, Morley et al. 2019). **Figure 12** shows the derived $^{12}C/^{13}C$ isotope

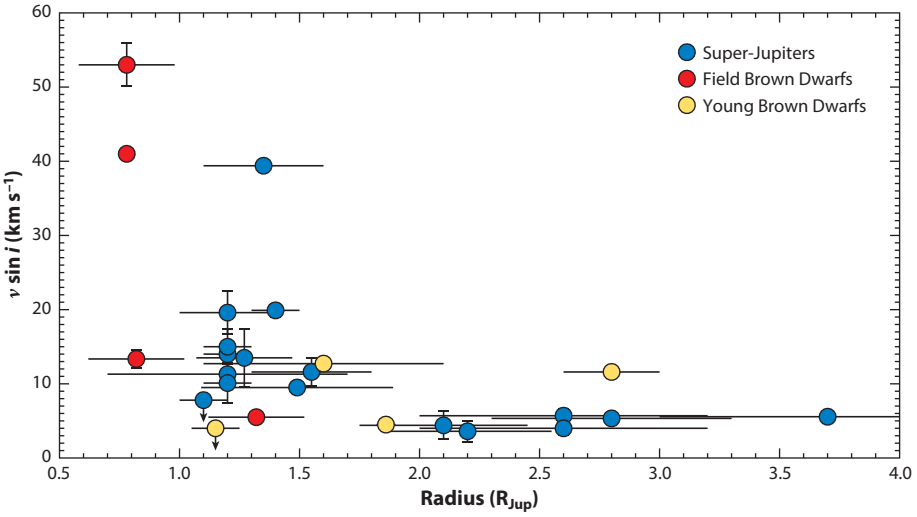

Figure 11

High-resolution spectroscopy measurements of $v \sin i$ as a function of estimated object radius for field brown dwarfs (*red*), young brown dwarfs (*yellow*) and super-Jupiters (*blue*). Data taken from de Regt et al. (2024), González Picos et al. (2024), Zhang et al. (2021, 2024b), Landman et al. (2024), Xuan et al. (2022, 2024a,b), Costes et al. (2024), Wang et al. (2021), Bryan et al. (2018, 2020b), and Hsu et al. (2024) and provided in **Supplemental Table 2**.

Supplemental Material >

ratios from HRS retrieval analysis for brown dwarfs, super-Jupiters, and hot Jupiters. Again, this is a very heterogeneous sample and could be biased in multiple ways. The $^{12}C/^{13}C$ ratio for VHS 1256b is derived from medium-resolution JWST spectroscopy, which also detects ^{17}O and ^{18}O (Gandhi et al. 2023a). The average isotope ratio in the interstellar medium and the Solar System are also shown in **Figure 12**. The first exoplanet isotope measured as presented by Zhang et al. (2021) showed the atmosphere of YSES 1b to be rich in carbon-13 with $^{12}C/^{13}C = 31^{+17}_{-10}$, but higher-quality HRS observations now point to $^{12}C/^{13}C = 88 \pm 13$ (Zhang et al. 2024a). Also, two independent HRS studies of GQ Lupi b point to significantly different isotope ratios. The implication is that these measurements are still challenging, that uncertainties may be underestimated, and/or that systematic effects are yet not well understood. Taking the measurements in **Figure 12** at face value, the super-Jupiters appear to have slightly lower carbon isotope ratios than the brown dwarfs, whereas the three hot Jupiters have even lower ratios. However, these latter measurements are presented as tentative detections and may suffer from detection bias. It is fair to say that it is too early to draw any conclusions but that a new avenue of exoplanet atmospheric characterization is opening up.

5. SYNERGIES WITH *JAMES WEBB SPACE TELESCOPE* SPECTROSCOPY OF EXOPLANETS

Only two years after the start of its science operations, it is clear that the JWST is revolutionizing the field of extrasolar planets. Although transmission spectroscopy of hot Jupiters has revealed previously undetected species such as CO_2 and SO_2 (e.g., Powell et al. 2024), it also pioneers detailed atmospheric characterization of smaller and cooler planets. For example, SO_2 and silicate clouds are detected in a warm Neptune (Dyrek et al. 2024), strong evidence is found for a secondary atmosphere around the hot rocky exoplanet 55 Cancri e (Hu et al. 2024), and mid-IR

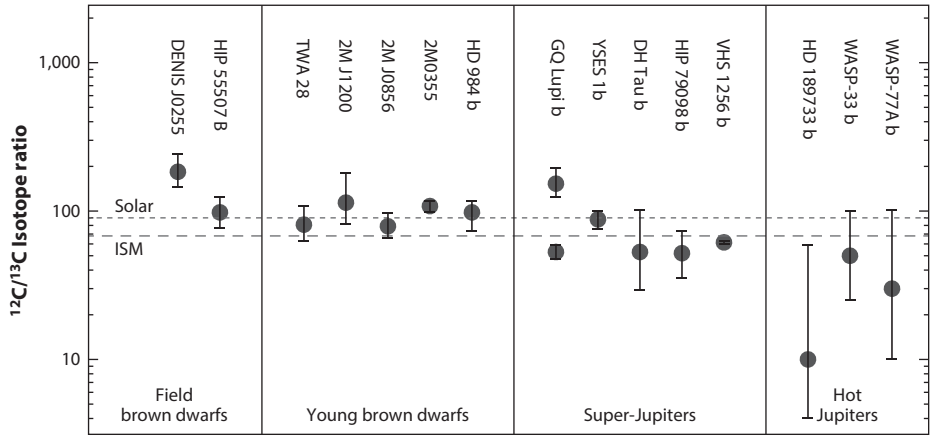

Figure 12

Carbon isotope ratios presented in the literature for field brown dwarfs, young brown dwarfs, super-Jupiters, and hot Jupiters. The dashed and dotted lines indicate the average isotope ratio in the interstellar medium and the Solar System, respectively. Data taken from de Regt et al. (2024), González Picos et al. (2024), Zhang et al. (2021, 2024b), Landman et al. (2024), Xuan et al. (2022, 2024a,b), Costes et al. (2024), Wang et al. (2021), Bryan et al. (2018, 2020b), and Hsu et al. (2024) and provided in **Supplemental Table 2**. Abbreviation: ISM, interstellar medium.

Supplemental Material >

secondary eclipse observations with MIRI (Mid-Infrared Instrument) are constraining the dayside temperatures of the Earth-sized planets in the TRAPPIST-1 system (e.g., Zieba et al. 2023).

The great sensitivity of JWST relative to ground-based observations, in particular at wavelengths beyond 2.5 μm, means that the enormous collecting area of the ELTs will likely be required for HRS to play a competitive role in the thermal IR. We discuss how HRS can break new ground in the era of the ELTs in the next section. However, there are exciting synergies with JWST with current 8–10-m-class telescopes and domains where ground-based HRS continues to provide uniquely new insights.

Some spectral regions can be particularly crowded with absorption features from a variety of species such that low-resolution spectroscopy cannot unambiguously identify the absorbing molecules or atoms. The optical–NIR spectra of UHJs are very rich in metals (see **Figure 6**), which are challenging to individually identify with JWST's limited spectral resolution. Also, the velocity structure of exospheric helium, as a probe of atmospheric loss process, is uniquely accessible with ground-based HRS. The spectral signature of CO, consisting of a series of regularly spaced lines, is particularly favorable for HRS. Although CO was the first molecule detected in the transmission spectrum of HD 209458b (Snellen et al. 2010), it is barely seen in JWST/NIRSpec transmission observations of the planet (Xue et al. 2024). Also, CO is not seen in JWST/NIRISS (Near Infrared Imager and Slitless Spectrograph) secondary eclipse observations of WASP-18b (Coulombe et al. 2023), whereas it is clearly detected in ground-based HRS observations with IGRINS (Immersion GRating INfrared Spectrometer) (Brogi et al. 2023), allowing for the planet's C/O ratio to be measured.

The study of minor isotopes has exciting synergetic opportunities between HRS and JWST observations. While ground-based HRS has so far focused on ^{13}CO, JWST observations have revealed $^{15}NH_3$ (Barrado et al. 2023) and ^{17}O and ^{18}O isotopes of CO (Gandhi et al. 2023a), and possibly deuterium (in CH_3D) is within reach (Morley et al. 2019). The future will tell whether trends in isotope ratios emerge that shed new light on planet formation and evolutionary processes.

The spectral resolution of JWST instrumentation is insufficient to directly probe any dynamics, but phase-curve analyses of close-in planets still provide crucial information on dayside-to-nightside heat distribution, heat transportation, and longitudinal distribution of molecular gases. These can be coupled to direct measurements of wind speeds and morning and/or evening terminator retrievals from HRS to build up a holistic picture of hot Jupiter atmospheres. In a similar way, JWST variability monitoring can be directly linked to HRS $v \sin i$ and line profile variation measurements to constrain cloud cover distributions and planet obliquities.

Although HRS preserves information on individual line profiles and probes atmospheres at relatively low pressures, JWST observations preserve continuum information more accurately, have generally a wider spectral range, and probe deeper parts of the atmosphere. Combining the two can be a powerful way to constrain a planet's properties (Brogi et al. 2017, Gandhi et al. 2019). Smith et al. (2024) used a joint retrieval framework on secondary-eclipse JWST and pre- and posteclipse HRS observations on the hot Jupiter WASP-77Ab, showing that both datasets are consistent and that molecular abundances as well as vertical thermal structure could be determined at higher precision than by using either dataset individually. It is also interesting to apply ground-based CC HRS techniques to medium-resolution JWST observations. Snellen et al. (2017) proposed to apply such a technique to MIRI medium-resolution spectroscopy spectra of Proxima Cen b to reveal potential signatures from CO_2, which seems technically within the realm of possibilities (Deming et al. 2024b). Esparza-Borges et al. (2023) apply CC techniques on WASP-39b NIRSpec data, showing it to be more powerful than a conventional analysis, unequivocally showing the presence of CO, and providing evidence for ^{13}CO.

It remains a fact that JWST is pushing exoplanet characterization to a regime that currently seems out of the reach of ground-based HRS. It remains to be seen how far HRS transmission spectroscopy can be pushed to cooler planets on wider orbits. The question is whether ground-based HRS observers should be more bold and daring. It is important to know whether detections of CO_2 and SO_2 are currently too difficult from the ground or whether simply nobody tried. Maybe HRS observers (and telescope allocation committees) have been too conservative and unwilling to invest significantly more observing time on individual targets to break new ground. The same can be argued for the new discoveries of young embedded planets, such as PDS 70 (Haffert et al. 2019, Cugno et al. 2021) and AB Aurigae (Currie et al. 2022), for which HRS observations could constrain the dynamics and chemistry of their accretion environments.

6. FUTURE OPPORTUNITIES WITH THE EXTREMELY LARGE TELESCOPES

As discussed in Section 2, with the advent of the ELTs, we will enter a new era of HRS exoplanet characterization. The increase in collecting area (and detection speed) of up to a factor of 25 will increase the sensitivity of HRS transmission and phase-curve observations by up to a factor of 5. It means that high-resolution emission and transmission spectra of hot gas-giant planets will be obtained that is of similar quality as those currently obtained for brown dwarfs (Prinoth et al. 2024b), but it also means that temporal information, e.g., during ingress, egress, or specific orbital phases, will provide detailed information of the temperature structure, gaseous content, and dynamics in specific areas of their atmospheres. Although transmission spectroscopy of cooler exoplanets often results in flat transmission spectra due to clouds and hazes, it is expected that ELT-HRS can probe such atmospheres above their clouds to determine their gaseous contents and climates (e.g., Gandhi et al. 2020, Hood et al. 2020, Grasser et al. 2024). Also, it may well be that HRS with the ELTs will break the degeneracies originating from stellar activity that currently plague JWST transmission observations (e.g., Deming et al. 2024a).

It is in high-contrast HRS where enormous gains will be made, increasing the detection speed by three orders of magnitude and unlocking exoplanets at unprecedentedly small angular distances from their host stars. Although METIS (Brandl et al. 2021), a first-generation instrument at the ELT, will have an $R = 100{,}000$ integral field and long-slit spectroscopy between 3 and 5 μm at near-maximum Strehl ratios, second-generation instrument ANDES (which will exhibit a small IFU) will serve the optical and NIR regime at similar spectral resolution (Marconi et al. 2022). Although current instrumentation is generally limited to such contrasts that it can only probe young planets that are still sufficiently warm from their formation, the ELTs are expected to push into the regime so that scattered light from planets around our nearest neighbors can be studied. Many such planets are already known to exist through RV or astrometric studies, and many more are expected from population statistics. The mid-IR detection of a temperate super-Jupiter around one of the most close-by solar-type stars, Epsilon Indi A, using JWST (Matthews et al. 2024a) is a milestone. Excitingly, its thermal emission at 10 μm is visible in archival VLT data. Knowing the orders-of-magnitude increase in sensitivity that will be achieved with the ELTs, such a planet can be detected within minutes of observing time. It may already be detectable at ∼4 μm using HRS with current telescopes to characterize the molecular content of its atmosphere, illustrating the enormous potential of the ELTs.

The ultimate goal for the ELTs, and arguably the exoplanet field as a whole, is to characterize Earth-like planets and establish whether they could be habitable and show signs of life. This involves a cascade of questions about temperate rocky planets: Do these planets have an atmosphere? What are their chemical constituents? What are their climates like? Is there any water? Are there biomarker gases present? Are these biomarkers indeed due to biological activity? This final question will be extremely challenging to address. Temperate rocky planets in red dwarf systems are the most accessible for characterization, and JWST is paving the way by addressing the first and possibly the second question above for a subset of the TRAPPIST-1 planets (e.g., Zieba et al. 2023). If their atmospheric conditions are favorable, HRS transmission spectroscopy with the ELT will be sensitive to molecular absorption including molecular oxygen, although the latter will be challenging (Snellen et al. 2013, Rodler & López-Morales 2014, Currie et al. 2023).

However, it is high-contrast spectroscopy that will be the real game changer for the characterization of other Earths. METIS HRS-IFU mode will be able to target Proxima Cen b and probe the atmosphere for H_2O, CO_2, and CH_4 in the L and M bands. If the atmosphere is water rich, deuterium and the D/H ratio may be determined via HDO measurements at 3.5 μm (Mollière & Snellen 2019) and shed light on its history of atmospheric loss. ANDES, with its small IFU mode, will determine its albedo over the optical and NIR, constrain cloud cover, and probe gaseous species, including molecular oxygen (Lovis et al. 2017, Palle et al. 2023, Vaughan et al. 2024).

The results of the first and second generations of ELT instrumentation will greatly depend on the specific properties of rocky planets around M dwarfs, such as their geometric albedo (reflected light is expected to dominate over thermal emission at <5 μm). Results on Proxima Cen b will also largely be governed by the contrast limits that can be reached with AO, which is more challenging at shorter wavelengths. Dedicated instrumentation will be needed to facilitate extreme AO for the ELTs at the level of the state-of-the-art HCI facilities at current 8–10-m telescopes. This instrumentation is currently being developed for the European ELT (the planetary camera and spectrograph or PCS) (Kasper et al. 2021) and the Giant Magellan Telescope (GMT) (the GMagAO-X) (Males et al. 2022). It is still an open question at what spectral resolution these instruments will operate. Landman et al. (2023) presented detailed simulations for gas giant planets and showed that medium resolution is optimal for this type of planet from a S/n point of view. However, in the case of reflected light, it is probably necessary to spectrally separate the Doppler-shifted planet spectrum from direct starlight to avoid confusion from near-identical telluric and

stellar features, pushing requirements to the high-resolution regime. It is envisaged that the high spectral and spatial resolution at extreme contrast levels will eventually allow the characterization of up to tens of temperate rocky planets around nearby M dwarfs (Hardegree-Ullman et al. 2024).

Current projections suggest that the 10^{9-10} contrasts needed to detect and characterize Earth-twins around solar-type stars will not be reached with ground-based instrumentation and will require space observatories such as the proposed Habitable Worlds Observatory (HWO; **https://habitableworldsobservatory.org/home**) or a space interferometer at mid-IR wavelengths (e.g., the LIFE mission; **https://life-space-mission.com**). It has been contemplated whether space-based HRS would be an interesting avenue to pursue, knowing the technical challenges. Evidently, the absence of telluric contamination removes an important reason to use HRS. While the dominant noise source for ground-based observations is that from leaked starlight, space-based observations will likely contend with detector noise. Hence, without new technologies that will significantly reduce detector noise, high spectral resolution (spreading the light over many more detector pixels) is less favorable. Taking these considerations into account, it is apparent that $R \sim$ 100–5,000 spectroscopy will have the largest discovery space and characterization power for Earth-twins (Wang et al. 2017) using HWO-type space observatories. The power of HRS is closely tied to its use with the largest ground-based telescopes.

DISCLOSURE STATEMENT

The author is not aware of any affiliations, memberships, funding, or financial holdings that might be perceived as affecting the objectivity of this review.

ACKNOWLEDGMENTS

The author is grateful for all the stimulating discussions with many colleagues. In particular, Michael Line, Matteo Brogi, Jayne Birkby, Paul Mollière, Sid Gandhi, Natalie Grasser, Dario Gónzalez Picos, Yapeng Zhang, and Sam de Regt are thanked for their careful reading of the manuscript and comments.

LITERATURE CITED

Allart R, Bourrier V, Lovis C, et al. 2018. *Science* 362(6421):1384–87
Allart R, Bourrier V, Lovis C, et al. 2019. *Astron. Astrophys.* 623:A58
Allart R, Pino L, Lovis C, et al. 2020. *Astron. Astrophys.* 644:A155
Azevedo Silva T, Demangeon ODS, Santos NC, et al. 2022. *Astron. Astrophys.* 666:L10
Barrado D, Mollière P, Patapis P, et al. 2023. *Nature* 624(7991):263–66
Basilicata M, Giacobbe P, Bonomo AS, et al. 2024. *Astron. Astrophys.* 686:A127
Baudino JL, Bézard B, Boccaletti A, et al. 2015. *Astron. Astrophys.* 582:A83
Bazinet L, Pelletier S, Benneke B, Salinas R, Mace GN. 2024. *Astron. J.* 167:206
Bello-Arufe A, Cabot SHC, Mendonça JM, Buchhave LA, Rathcke AD. 2022. *Astron. J.* 163(2):96
Bello-Arufe A, Knutson HA, Mendonça JM, et al. 2023. *Ap. J.* 166(2):69
Beltz H, Rauscher E, Roman MT, Guilliat A. 2022. *Astron. J.* 163(1):35
Ben-Yami M, Madhusudhan N, Cabot SHC, et al. 2020. *Ap. J. Lett.* 897(1):L5
Benneke B, Wong I, Piaulet C, et al. 2019. *Ap. J. Lett.* 887(1):L14
Bernath PF. 2020. *J. Quant. Spectrosc. Radiat. Transf.* 240:106687
Birkby JL. 2018. arXiv:1806.04617 [astro-ph.EP]
Birkby JL, de Kok RJ, Brogi M, Schwarz H, Snellen IAG. 2017. *Ap. J.* 153(3):138
Birkby JL, de Kok RJ, Brogi M, et al. 2013. *MNRAS* 436:L35–39
Blain D, Landman R, Mollière P, Dittmann J. 2024. *Astron. Astrophys.* 690:A63
Borsa F, Allart R, Casasayas-Barris N, et al. 2021a. *Astron. Astrophys.* 645:A24

Borsa F, Fossati L, Koskinen T, Young ME, Shulyak D. 2021b. *Nat. Astron.* 6:226–31
Borsa F, Rainer M, Bonomo AS, et al. 2019. *Astron. Astrophys.* 631:A34
Borsato NW, Hoeijmakers HJ, Prinoth B, et al. 2023. *Astron. Astrophys.* 673:A158
Boucher A, Darveau-Bernier A, Pelletier S, et al. 2021. *Ap. J.* 162(6):233
Boucher A, Lafreniére D, Pelletier S, et al. 2023. *MNRAS* 522(4):5062–83
Bourrier V, Ehrenreich D, Lendl M, et al. 2020. *Astron. Astrophys.* 635:A205
Bowesman CA, Yurchenko SN, Tennyson J. 2024. *Mol. Phys.* 122(7–8):e2255299
Bowler BP, Liu MC, Dupuy TJ, Cushing MC. 2010. *Ap. J.* 723(1):850–68
Brandl B, Bettonvil F, van Boekel R, et al. 2021. *Messenger* 182:22–26
Brogi M, de Kok RJ, Albrecht S, et al. 2016. *Ap. J.* 817(2):106
Brogi M, de Kok RJ, Birkby JL, Schwarz H, Snellen IAG. 2014. *Astron. Astrophys.* 565:A124
Brogi M, Emeka-Okafor V, Line MR, et al. 2023. *Ap. J.* 165(3):91
Brogi M, Line M, Bean J, Désert JM, Schwarz H. 2017. *Ap. J. Lett.* 839(1):L2
Brogi M, Line MR. 2019. *Ap. J.* 157(3):114
Brogi M, Snellen IAG, de Kok RJ, et al. 2012. *Nature* 486(7404):502–4
Brogi M, Snellen IAG, de Kok RJ, et al. 2013. *Ap. J.* 767(1):27
Brown TM. 2001. *Ap. J.* 553(2):1006–26
Bryan ML, Benneke B, Knutson HA, Batygin K, Bowler BP. 2018. *Nat. Astron.* 2:138–44
Bryan ML, Chiang E, Bowler BP, et al. 2020a. *Astron. J.* 159(4):181
Bryan ML, Ginzburg S, Chiang E, et al. 2020b. *Ap. J.* 905(1):37
Burningham B, Marley MS, Line MR, et al. 2017. *MNRAS* 470(1):1177–97
Burrows A, Hubeny I, Budaj J, Knutson HA, Charbonneau D. 2007. *Ap. J. Lett.* 668(2):L171–74
Cabot SHC, Madhusudhan N, Hawker GA, Gandhi S. 2019. *MNRAS* 482(4):4422–36
Carteret Y, Bourrier V, Dethier W. 2024. *Astron. Astrophys.* 683:A63
Casasayas-Barris N, Palle E, Stangret M, et al. 2021. *Astron. Astrophys.* 647:A26
Casasayas-Barris N, Pallé E, Yan F, et al. 2019. *Astron. Astrophys.* 628:A9
Cauley PW, Wang J, Shkolnik EL, et al. 2021. *Ap. J.* 161(3):152
Cegla HM, Lovis C, Bourrier V, et al. 2016. *Astron. Astrophys.* 588:A127
Charbonneau D, Allen LE, Megeath ST, et al. 2005. *Ap. J.* 626(1):523–29
Charbonneau D, Brown TM, Latham DW, Mayor M. 2000. *Ap. J. Lett.* 529(1):L45–48
Charbonneau D, Brown TM, Noyes RW, Gilliland RL. 2002. *Ap. J.* 568(1):377–84
Charbonneau D, Noyes RW, Korzennik SG, et al. 1999. *Ap. J. Lett.* 522(2):L145–148
Chauvin G, Lagrange AM, Dumas C, et al. 2004. *Astron. Astrophys.* 425:L29–32
Chazelas B, Lovis C, Blind N, et al. 2020. *Proc. SPIE Conf. Ser.* 11448:1144875
Chen G, Casasayas-Barris N, Pallé E, et al. 2020a. *Astron. Astrophys.* 642:A54
Chen G, Casasayas-Barris N, Pallé E, et al. 2020b. *Astron. Astrophys.* 635:A171
Cheverall C, Madhusudhan N. 2024. arXiv:2403.18894 [astro-ph.EP]
Cheverall CJ, Madhusudhan N, Holmberg M. 2023. *MNRAS* 522(1):661–77
Collier Cameron A, Horne K, Penny A, James D. 1999. *Nature* 402(6763):751–55
Cont D, Yan F, Reiners A, et al. 2021. *Astron. Astrophys.* 651:A33
Cont D, Yan F, Reiners A, et al. 2022a. *Astron. Astrophys.* 657:L2
Cont D, Yan F, Reiners A, et al. 2022b. *Astron. Astrophys.* 668:A53
Cooper CS, Showman AP. 2006. *Ap. J.* 649(2):1048–63
Costes JC, Xuan JW, Vigan A, et al. 2024. *Astron. Astrophys.* 686:A294
Coulombe LP, Benneke B, Challener R, et al. 2023. *Nature* 620(7973):292–98
Cristo E, Santos NC, Demangeon O, et al. 2022. *Astron. Astrophys.* 660:A52
Crossfield IJM. 2014. *Astron. Astrophys.* 566:A130
Cugno G, Patapis P, Stolker T, et al. 2021. *Astron. Astrophys.* 653:A12
Currie MH, Meadows VS, Rasmussen KC. 2023. *Planet. Sci. J.* 4(5):83
Currie T, Lawson K, Schneider G, et al. 2022. *Nat. Astron.* 6:751–59
Czesla S, Klocová T, Khalafinejad S, Wolter U, Schmitt JHMM. 2015. *Astron. Astrophys.* 582:A51
de Kok RJ, Brogi M, Snellen IAG, et al. 2013. *Astron. Astrophys.* 554:A82

de Regt S, Gandhi S, Snellen IAG, et al. 2024. *Astron. Astrophys.* 688:A116
de Regt S, Kesseli AY, Snellen IAG, Merritt SR, Chubb KL. 2022. *Astron. Astrophys.* 661:A109
Deibert EK, de Mooij EJW, Jayawardhana R, et al. 2021. *Ap. J. Lett.* 919(2):L15
Delorme JR, Jovanovic N, Echeverri D, et al. 2021. *J. Astron. Telesc. Instrum. Syst.* 7:035006
Deming D, Brown TM, Charbonneau D, Harrington J, Richardson LJ. 2005a. *Ap. J.* 622(2):1149–59
Deming D, Currie M, Meadows V, Peacock S. 2024a. *Bull. Am. Astron. Soc.* 56(7):407.05. Abstr.
Deming D, Fu G, Bouwman J, et al. 2024b. *Publ. Astron. Soc. Pac.* 136(8):084402
Deming D, Seager S, Richardson LJ, Harrington J. 2005b. *Nature* 434(7034):740–43
Deming D, Wilkins A, McCullough P, et al. 2013. *Ap. J.* 774(2):95
Di Gloria E, Snellen IAG, Albrecht S. 2015. *Astron. Astrophys.* 580:A84
Dreizler S, Reiners A, Homeier D, Noll M. 2009. *Astron. Astrophys.* 499(2):615–21
Dupuy TJ, Liu MC, Evans EL, et al. 2023. *MNRAS* 519(2):1688–94
Dyrek A, Min M, Decin L, et al. 2024. *Nature* 625(7993):51–54
Ehrenreich D, Bourrier V, Wheatley PJ, et al. 2015. *Nature* 522(7557):459–61
Ehrenreich D, Lovis C, Allart R, et al. 2020. *Nature* 580(7805):597–601
Esparza-Borges E, López-Morales M, Adams Redai JI, et al. 2023. *Ap. J. Lett.* 955(1):L19
Finnerty L, Schofield T, Sappey B, et al. 2023. *Ap. J.* 166(1):31
Fisher C, Hoeijmakers HJ, Kitzmann D, et al. 2020. *Ap. J.* 159(5):192
Flagg L, Turner JD, Deibert E, et al. 2023. *Ap. J. Lett.* 953(2):L19
Folha DFM, Emerson JP. 1999. *Astron. Astrophys.* 352:517–31
Fortney JJ, Lodders K, Marley MS, Freedman RS. 2008. *Ap. J.* 678(2):1419–35
Fossati L, Biassoni F, Cappello GM, et al. 2023. *Astron. Astrophys.* 676:A99
Gandhi S, Brogi M, Webb RK. 2020. *MNRAS* 498(1):194–204
Gandhi S, de Regt S, Snellen I, et al. 2023a. *Ap. J. Lett.* 957(2):L36
Gandhi S, Kesseli A, Snellen I, et al. 2022. *MNRAS* 515(1):749–66
Gandhi S, Kesseli A, Zhang Y, et al. 2023b. *Ap. J.* 165(6):242
Gandhi S, Madhusudhan N. 2018. *MNRAS* 474(1):271–88
Gandhi S, Madhusudhan N, Hawker G, Piette A. 2019. *Astron. J.* 158(6):228
Giacobbe P, Brogi M, Gandhi S, et al. 2021. *Nature* 592(7853):205–8
Gibson NP, de Mooij EJW, Evans TM, et al. 2019. *MNRAS* 482(1):606–15
Gibson NP, Merritt S, Nugroho SK, et al. 2020. *MNRAS* 493(2):2215–28
Gibson NP, Nugroho SK, Lothringer J, Maguire C, Sing DK. 2022. *MNRAS* 512(3):4618–38
González Picos D, Snellen IAG, de Regt S, et al. 2024. *Astron. Astrophys.* 689:A212
González Picos D, Snellen IAG, de Regt S, et al. 2025. *Astron. Astrophys.* 693:A298
Gordon IE, Rothman LS, Hill C, et al. 2017. *J. Quant. Spectrosc. Radiat. Transf.* 203:3–69
Grasser N, Snellen IAG, Landman R, Picos DG, Gandhi S. 2024. *Astron. Astrophys.* 688:A191
GRAVITY Collab., Nowak M, Lacour S, et al. 2020. *Astron. Astrophys.* 633:A110
Gray DF. 1997. *Nature* 385(6619):795–96
Guillot T. 2010. *Astron. Astrophys.* 520:A27
Guilluy G, Sozzetti A, Brogi M, et al. 2019. *Astron. Astrophys.* 625:A107
Gully-Santiago M, Morley CV, Luna J, et al. 2024. *Astron. J.* 167(4):142
Haffert SY, Bohn AJ, de Boer J, et al. 2019. *Nat. Astron.* 3:749–54
Hardegree-Ullman KK, Apai D, Haffert SY, et al. 2024. arXiv:2405.11423 [astro-ph.EP]
Hargreaves RJ, Gordon IE, Rey M, et al. 2020. *Ap. J. Suppl.* 247(2):55
Hawker GA, Madhusudhan N, Cabot SHC, Gandhi S. 2018. *Ap. J. Lett.* 863(1):L11
Herman MK, de Mooij EJW, Jayawardhana R, Brogi M. 2020. *Ap. J.* 160(2):93
Hoeijmakers HJ, Cabot SHC, Zhao L, et al. 2020. *Astron. Astrophys.* 641:A120
Hoeijmakers HJ, de Kok RJ, Snellen IAG, et al. 2015. *Astron. Astrophys.* 575:A20
Hoeijmakers HJ, Ehrenreich D, Heng K, et al. 2018a. *Nature* 560(7719):453–55
Hoeijmakers HJ, Ehrenreich D, Kitzmann D, et al. 2019. *Astron. Astrophys.* 627:A165
Hoeijmakers HJ, Kitzmann D, Morris BM, et al. 2022. arXiv:2210.12847 [astro-ph.EP]
Hoeijmakers HJ, Snellen IAG, van Terwisga SE. 2018b. *Astron. Astrophys.* 610:A47

Holmberg M, Madhusudhan N. 2022. *Ap. J.* 164(3):79
Hood CE, Fortney JJ, Line MR, et al. 2020. *Astron. J.* 160(5):198
Hood T, Debras F, Moutou C, et al. 2024. *Astron. Astrophys.* 687:A119
Hsu CC, Wang JJ, Xuan JW, Ruffio JB, Morris E, et al. 2024. *Ap. J.* 971(1):9
Hu R, Bello-Arufe A, Zhang M, et al. 2024. *Nature* 630(8017):609–612
Irwin PGJ, Teanby NA, de Kok R, et al. 2008. *J. Quant. Spectrosc. Radiat. Transf.* 109:1136–50
Jiang Z, Wang W, Zhao G, et al. 2023. *Ap. J.* 165(6):230
Kasper M, Cerpa Urra N, Pathak P, et al. 2021. *Messenger* 182:38–43
Kawahara H, Hirano T. 2014. arXiv:1409.5740 [astro-ph.EP]
Kawahara H, Kawashima Y, Masuda K, et al. 2022. *Ap. J. Suppl.* 258(2):31
Kempton EMR, Perna R, Heng K. 2014. *Ap. J.* 795(1):24
Kesseli AY, Snellen IAG. 2021. *Ap. J. Lett.* 908(1):L17
Kesseli AY, Snellen IAG, Alonso-Floriano FJ, Mollière P, Serindag DB. 2020. *Ap. J.* 160(5):228
Kesseli AY, Snellen IAG, Casasayas-Barris N, Mollière P, Sánchez-López A. 2022. *Ap. J.* 163(3):107
Kitzmann D, Heng K, Rimmer PB, et al. 2018. *Ap. J.* 863(2):183
Knutson HA, Charbonneau D, Allen LE, Burrows A, Megeath ST. 2008. *Ap. J.* 673(1):526–31
Knutson HA, Charbonneau D, Allen LE, et al. 2007. *Nature* 447(7141):183–86
Konopacky QM, Barman TS, Macintosh BA, Marois C. 2013. *Science* 339(6126):1398–401
Kotani T, Kawahara H, Ishizuka M, et al. 2020. *Proc. SPIE Conf. Ser.* 11448:1144878
Kreidberg L, Bean JL, Désert JM, et al. 2014. *Nature* 505(7481):69–72
Lagrange AM, Bonnefoy M, Chauvin G, et al. 2010. *Science* 329(5987):57–59
Landman R, Sánchez-López A, Mollière P, et al. 2021. *Astron. Astrophys.* 656:A119
Landman R, Snellen IAG, Keller CU, et al. 2023. *Astron. Astrophys.* 675:A157
Landman R, Stolker T, Snellen IAG, et al. 2024. *Astron. Astrophys.* 682:A48
Langeveld AB, Madhusudhan N, Cabot SHC. 2022. *MNRAS* 514(4):5192–213
Lecavelier Des Etangs A, Ehrenreich D, Vidal-Madjar A, et al. 2010. *Astron. Astrophys.* 514:A72
Leigh C, Collier Cameron A, Horne K, Penny A, James D. 2003. *MNRAS* 344(4):1271–82
Lesjak F, Nortmann L, Yan F, et al. 2023. *Astron. Astrophys.* 678:A23
Line MR, Brogi M, Bean JL, et al. 2021. *Nature* 598(7882):580–84
Line MR, Fortney JJ, Marley MS, Sorahana S. 2014. *Ap. J.* 793(1):33
Lothringer JD, Barman T. 2019. *Ap. J.* 876(1):69
Louden T, Wheatley PJ. 2015. *Ap. J. Lett.* 814(2):L24
Lovis C, Snellen I, Mouillet D, et al. 2017. *Astron. Astrophys.* 599:A16
Madhusudhan N. 2019. *Annu. Rev. Astron. Astrophys.* 57:617–63
Madhusudhan N, Seager S. 2009. *Ap. J.* 707(1):24–39
Maguire C, Gibson NP, Nugroho SK, et al. 2023. *MNRAS* 519(1):1030–48
Maimone MC, Brogi M, Chiavassa A, et al. 2022. *Astron. Astrophys.* 667:A106
Males JR, Close LM, Haffert SY, et al. 2022. *Proc. SPIE Conf. Ser.* 12185:121854J
Malik M, Grosheintz L, Mendonça JM, et al. 2017. *Astron. J.* 153(2):56
Marconi A, Abreu M, Adibekyan V, et al. 2022. *Proc. SPIE Conf. Ser.* 12184:1218424
Marley MS, Robinson TD. 2015. *Annu. Rev. Astron. Astrophys.* 53:279–323
Marois C, Macintosh B, Barman T, et al. 2008. *Science* 322(5906):1348–52
Martins JHC, Santos NC, Figueira P, et al. 2015. *Astron. Astrophys.* 576:A134
Matthews E, Carter A, Pathak Pea. 2024a. *Nature* 633(8031):789–92
Matthews SM, Watson CA, de Mooij EJW, et al. 2024b. *MNRAS* 531(3):3800–14
Mawet D, Wizinowich P, Dekany R, et al. 2016. *Proc. SPIE Conf. Ser.* 9909:99090D
Mayor M, Queloz D. 1995. *Nature* 378(6555):355–59
McCann J, Murray-Clay RA, Kratter K, Krumholz MR. 2019. *Ap. J.* 873(1):89
McKemmish LK, Masseron T, Hoeijmakers HJ, et al. 2019. *MNRAS* 488(2):2836–54
Merritt SR, Gibson NP, Nugroho SK, et al. 2021. *MNRAS* 506(3):3853–71
Miller-Ricci Kempton E, Rauscher E. 2012. *Ap. J.* 751(2):117
Mollière P, Wardenier JP, van Boekel R, et al. 2019. *Astron. Astrophys.* 627:A67

Mollière P, Snellen IAG. 2019. *Astron. Astrophys.* 622:A139
Moran SE, Stevenson KB, Sing DK, et al. 2023. *Ap. J. Lett.* 948(1):L11
Morley CV, Skemer AJ, Miles BE, et al. 2019. *Ap. J. Lett.* 882(2):L29
Mounzer D, Lovis C, Seidel JV, et al. 2022. *Astron. Astrophys.* 668:A1
Moutou C, Coustenis A, Schneider J, et al. 2001. *Astron. Astrophys.* 371:260–66
Nortmann L, Pallé E, Salz M, et al. 2018. *Science* 362(6421):1388–91
Nugroho SK, Gibson NP, de Mooij EJW, et al. 2020a. *Ap. J. Lett.* 898(2):L31
Nugroho SK, Gibson NP, de Mooij EJW, et al. 2020b. *MNRAS* 496(1):504–22
Nugroho SK, Kawahara H, Gibson NP, et al. 2021. *Ap. J. Lett.* 910(1):L9
Nugroho SK, Kawahara H, Masuda K, et al. 2017. *Ap. J.* 154(6):221
Öberg KI, Facchini S, Anderson DE. 2023. *Annu. Rev. Astron. Astrophys.* 61:287–328
Öberg KI, Murray-Clay R, Bergin EA. 2011. *Ap. J. Lett.* 743(1):L16
Oklopčić A. 2019. *Ap. J.* 881(2):133
Oklopčić A, Hirata CM. 2018. *Ap. J. Lett.* 855(1):L11
Pai Asnodkar A, Wang J, Eastman JD, et al. 2022. *Ap. J.* 163(4):155
Palle E, Biazzo K, Bolmont E, et al. 2023. arXiv:2311.17075 [astro-ph.IM]
Parmentier V, Showman AP, Lian Y. 2013. *Astron. Astrophys.* 558:A91
Pelletier S, Benneke B, Ali-Dib M, et al. 2023. *Nature* 619(7970):491–94
Pelletier S, Benneke B, Darveau-Bernier A, et al. 2021. *Ap. J.* 162(2):73
Perryman MAC. 2000. *Rep. Prog. Phys.* 63(8):1209–72
Pino L, Brogi M, Désert JM, et al. 2022. *Astron. Astrophys.* 668:A176
Pino L, Désert JM, Brogi M, et al. 2020. *Ap. J. Lett.* 894(2):L27
Piskorz D, Buzard C, Line MR, et al. 2018. *Ap. J.* 156(3):133
Powell D, Feinstein AD, Lee EKH, et al. 2024. *Nature* 626(8001):979–83
Prinoth B, Hoeijmakers HJ, Morris BM, et al. 2024a. *Astron. Astrophys.* 685:A60
Prinoth B, Hoeijmakers HJ, Pelletier S, et al. 2023. *Astron. Astrophys.* 678:A182
Prinoth B, Sedaghati E, Seidel JV, et al. 2024b. *Astron. J.* 168(3):133
Rahmati H, Czesla S, Khalafinejad S, Mollière P. 2022. *Astron. Astrophys.* 668:A24
Ramkumar S, Gibson NP, Nugroho SK, Maguire C, Fortune M. 2023. *MNRAS* 525(2):2985–3005
Rauscher E, Menou K. 2010. *Ap. J.* 714(2):1334–42
Redfield S, Endl M, Cochran WD, Koesterke L. 2008. *Ap. J. Lett.* 673(1):L87–90
Rey M, Nikitin AV, Babikov YL, Tyuterev VG. 2016. *J. Mol. Spectrosc.* 327:138–58
Riaud P, Schneider J. 2007. *Astron. Astrophys.* 469(1):355–61
Rodler F, Kürster M, Barnes JR. 2013. *MNRAS* 432(3):1980–88
Rodler F, López-Morales M. 2014. *Ap. J.* 781(1):54
Rodler F, Lopez-Morales M, Ribas I. 2012. *Ap. J. Lett.* 753(1):L25
Ruffio JB, Horstman K, Mawet D, et al. 2023. *Astron. J.* 165(3):113
Ruffio JB, Macintosh B, Konopacky QM, et al. 2019. *Astron. J.* 158(5):200
Santos NC, Cristo E, Demangeon O, et al. 2020. *Astron. Astrophys.* 644:A51
Schwarz H, Brogi M, de Kok R, Birkby J, Snellen I. 2015. *Astron. Astrophys.* 576:A111
Schwarz H, Ginski C, de Kok RJ, et al. 2016. *Astron. Astrophys.* 593:A74
Seager S, Sasselov DD. 2000. *Ap. J.* 537(2):916–21
Seidel JV, Borsa F, Pino L, et al. 2023a. *Astron. Astrophys.* 673:A125
Seidel JV, Cegla HM, Doyle L, Lafarga M, Brogi M, et al. 2022. *MNRAS* 513(1):L15–19
Seidel JV, Ehrenreich D, Allart R, et al. 2021. *Astron. Astrophys.* 653:A73
Seidel JV, Ehrenreich D, Pino L, et al. 2020. *Astron. Astrophys.* 633:A86
Seidel JV, Prinoth B, Knudstrup E, et al. 2023b. *Astron. Astrophys.* 678:A150
Serindag DB, Nugroho SK, Mollière P, et al. 2021. *Astron. Astrophys.* 645:A90
Showman AP, Cooper CS, Fortney JJ, Marley MS. 2008. *Ap. J.* 682(1):559–76
Showman AP, Fortney JJ, Lewis NK, Shabram M. 2013. *Ap. J.* 762(1):24
Sing DK, Fortney JJ, Nikolov N, et al. 2016. *Nature* 529(7584):59–62
Sing DK, Pont F, Aigrain S, et al. 2011. *MNRAS* 416(2):1443–55

Sing DK, Wakeford HR, Showman AP, et al. 2015. *MNRAS* 446(3):2428–43
Smith PCB, Line MR, Bean JL, et al. 2024. *Astron. J.* 167(3):110
Sánchez-López A, Landman R, Mollière P, et al. 2022a. *Astron. Astrophys.* 661:A78
Sánchez-López A, Lin L, Snellen IAG, et al. 2022b. *Astron. Astrophys.* 666:L1
Snellen I, de Kok R, Birkby JL, et al. 2015. *Astron. Astrophys.* 576:A59
Snellen IAG. 2004. *MNRAS* 353(1):L1–6
Snellen IAG, Albrecht S, de Mooij EJW, Le Poole RS. 2008. *Astron. Astrophys.* 487(1):357–62
Snellen IAG, Brandl BR, de Kok RJ, et al. 2014. *Nature* 509(7498):63–65
Snellen IAG, de Kok RJ, de Mooij EJW, Albrecht S. 2010. *Nature* 465(7301):1049–51
Snellen IAG, de Kok RJ, le Poole R, Brogi M, Birkby J. 2013. *Ap. J.* 764(2):182
Snellen IAG, Désert JM, Waters LBFM, et al. 2017. *Astron. J.* 154(2):77
Sousa-Silva C, Al-Refaie AF, Tennyson J, Yurchenko SN. 2015. *MNRAS* 446(3):2337–47
Spake JJ, Sing DK, Evans TM, et al. 2018. *Nature* 557(7703):68–70
Sparks WB, Ford HC. 2002. *Ap. J.* 578(1):543–64
Spring EF, Birkby JL, Pino L, et al. 2022. *Astron. Astrophys.* 659:A121
Stangret M, Casasayas-Barris N, Pallé E, et al. 2020. *Astron. Astrophys.* 638:A26
Stangret M, Casasayas-Barris N, Pallé E, et al. 2022. *Astron. Astrophys.* 662:A101
Tabernero HM, Zapatero Osorio MR, Allart R, et al. 2021. *Astron. Astrophys.* 646:A158
Tamuz O, Mazeh T, Zucker S. 2005. *MNRAS* 356(4):1466–70
Tennyson J, Yurchenko SN. 2021. *Astron. Geophys.* 62(6):6.16–21
Tinetti G, Vidal-Madjar A, Liang MC, et al. 2007. *Nature* 448(7150):169–71
Tremblin P, Padioleau T, Phillips MW, et al. 2019. *Ap. J.* 876(2):144
Tyler D, Petigura EA, Oklopčić A, David TJ. 2024. *Ap. J.* 960(2):123
van Sluijs L, Birkby JL, Lothringer J, et al. 2023. *MNRAS* 522(2):2145–70
Vaughan SR, Birkby JL, Thatte N, et al. 2024. *MNRAS* 528(2):3509–22
Vidal-Madjar A, Désert JM, Lecavelier des Etangs A, et al. 2004. *Ap. J. Lett.* 604(1):L69–72
Vidal-Madjar A, Lecavelier des Etangs A, et al. 2003. *Nature* 422(6928):143–46
Vigan A, El Morsy M, Lopez M, et al. 2024. *Astron. Astrophys.* 682:A16
Wang J, Mawet D, Ruane G, Hu R, Benneke B. 2017. *Ap. J.* 153(4):183
Wang JJ, Ruffio JB, Morris E, et al. 2021. *Astron. J.* 162(4):148
Wardenier JP, Parmentier V, Lee EKH, Line MR, Gharib-Nezhad E. 2021. *MNRAS* 506(1):1258–83
Watson CA, de Mooij EJW, Steeghs D, et al. 2019. *MNRAS* 490(2):1991–2006
Wiedemann G, Deming D, Bjoraker G. 2001. *Ap. J.* 546(2):1068–74
Wolszczan A, Frail DA. 1992. *Nature* 355(6356):145–47
Wyttenbach A, Lovis C, Ehrenreich D, et al. 2017. *Astron. Astrophys.* 602:A36
Wyttenbach A, Mollière P, Ehrenreich D, et al. 2020. *Astron. Astrophys.* 638:A87
Xuan JW, Hsu CC, Finnerty L, Wang J, Ruffio JB, et al. 2024a. *Ap. J.* 970(1):71
Xuan JW, Wang J, Finnerty L, Horstman K, Grimm S, et al. 2024b. *Ap. J.* 962(1):10
Xuan JW, Wang J, Ruffio JB, et al. 2022. *Ap. J.* 937(2):54
Xue Q, Bean JL, Zhang M, et al. 2024. *Ap. J. Lett.* 963(1):L5
Yan F, Casasayas-Barris N, Molaverdikhani K, et al. 2019. *Astron. Astrophys.* 632:A69
Yan F, Henning T. 2018. *Nat. Astron.* 2:714–18
Yan F, Nortmann L, Reiners A, et al. 2023. *Astron. Astrophys.* 672:A107
Yan F, Pallé E, Fosbury RAE, Petr-Gotzens MG, Henning T. 2017. *Astron. Astrophys.* 603:A73
Yan F, Pallé E, Reiners A, et al. 2020. *Astron. Astrophys.* 640:L5
Yan F, Pallé E, Reiners A, et al. 2022a. *Astron. Astrophys.* 661:L6
Yan F, Reiners A, Pallé E, et al. 2022b. *Astron. Astrophys.* 659:A7
Yan F, Wyttenbach A, Casasayas-Barris N, et al. 2021. *Astron. Astrophys.* 645:A22
Yang Y, Chen G, Wang S, Yan F. 2024. *Ap. J.* 167(1):36
Zahnle KJ, Marley MS. 2014. *Ap. J.* 797(1):41
Zhang M, Chachan Y, Kempton EMR, Knutson HA. 2019. *Publ. Astron. Soc. Pac.* 131(997):034501
Zhang M, Knutson HA, Dai F, et al. 2023. *Astron. J.* 165(2):62

Zhang Y, González Picos D, de Regt S, et al. 2024a. *Astron. J.* 168:246
Zhang Y, Snellen IAG, Bohn AJ, et al. 2021. *Nature* 595(7867):370–72
Zhang Y, Snellen IAG, Mollière P. 2021. *Astron. Astrophys.* 656:A76
Zhang Y, Snellen IAG, Mollière P, et al. 2020. *Astron. Astrophys.* 641:A161
Zhang Y, Snellen IAG, Wyttenbach A, et al. 2022. *Astron. Astrophys.* 666:A47
Zhang Y, Xuan JW, Mawet D, et al. 2024b. *Astron. J.* 168(3):131
Zhang Z, Mollière P, Hawkins K, et al. 2023a. *Astron. J.* 166(5):198
Zhang Z, Morley CV, Gully-Santiago M, et al. 2023b. *Sci. Adv.* 9(23):eadf8736
Zieba S, Kreidberg L, Ducrot E, et al. 2023. *Nature* 620(7975):746–49
Zhou G, Bayliss DDR. 2012. *MNRAS* 426(3):2483–88
Žák J, Kabáth P, Boffin HMJ, Ivanov VD, Skarka M. 2019. *Ap. J.* 158(3):120